Title

Tuning the Metabolic Stability of Visual Cycle Modulators through Modification of an RPE65 Recognition Motif.

Permalink

https://escholarship.org/uc/item/985043nx

Journal

Journal of medicinal and pharmaceutical chemistry, 66(12)

Authors

Bassetto, Marco

Zaluski, Jordan

Li, Bowen

et al.

Publication Date

2023-06-22

DOI

10.1021/acs.jmedchem.3c00461

Peer reviewed

Tuning the metabolic stability of visual cycle modulators through modification of an RPE65 recognition motif

Marco Bassetto[1,2,5,*], **Jordan Zaluski**[3,*], **Bowen Li**[3], **Jianye Zhang**[2], **Mohsen Badiee**[3], **Philip Kiser**[1,2,4,5,#], **Gregory P. Tochtrop**[3,#]

[1]Department of Physiology and Biophysics, School of Medicine, University of California-Irvine, Irvine, California 92697, USA

[2]Department of Ophthalmology, Gavin Herbert Eye Institute, Center for Translational Vision Research, School of Medicine, University of California – Irvine, Irvine, CA 92697, USA

[3]Department of Chemistry, Case Western Reserve University, Cleveland, Ohio 44106, USA

[4]Department of Clinical Pharmacy Practice, School of Pharmacy and Pharmaceutical Sciences, University of California – Irvine, Irvine, CA 92697, USA

[5]Research Service, VA Long Beach Healthcare System, Long Beach, CA 90822, USA

Abstract

In the eye, the isomerization of all-*trans*-retinal to 11-*cis*-retinal is accomplished by a metabolic pathway termed the visual cycle that is critical for vision. RPE65 is the essential *trans-cis* isomerase of this pathway. Emixustat, a retinoid-mimetic RPE65 inhibitor, was developed as a therapeutic visual cycle modulator and used for the treatment of retinopathies. However, pharmacokinetic liabilities limit its further development including: 1) metabolic deamination of the γ-amino-α-aryl alcohol which mediates targeted RPE65 inhibition, and 2) unwanted long-lasting RPE65 inhibition. We sought to address these issues by more broadly defining the structure-activity relationships of the RPE65 recognition motif via the synthesis of a family of novel derivatives, which were tested *in vitro* and *in vivo* for RPE65 inhibition. We identified a potent secondary amine derivative with resistance to deamination and preserved RPE65 inhibitory activity. Our data provide insights into activity-preserving modifications of the emixustat molecule that can be employed to tune its pharmacological properties.

Keywords

retinopathy; visual cycle; Stargardt disease; VAP-1; inhibitor; RPE65

INTRODUCTION:

The concerted work of two molecular pathways is at the base of vision. First, phototransduction amplifies the signal derived from the capture of photons by a

[#]To whom correspondence should be addressed.
[*]These authors contributed equally to this work.

chromophore, 11-*cis*-retinal (11cRAL), covalently bound to visual opsins in the rod and cone photoreceptor cells.[1] Second, the (retinoid) visual cycle, a multi-enzymatic process based largely within the retinal pigment epithelium (RPE), regenerates the spent chromophore, all-*trans*-retinal (RAL), to its 11-*cis* configuration (Figure 1A).[2] In addition, an incompletely defined cone/Müller cell pathway[3] and the retinal G-coupled protein receptor (RGR)-mediate non-classical[4] visual cycle activity that also supports rod and cone function.[5]

The classical visual cycle is essential to sustain phototransduction over time; however, compelling data indicate that this pathway can also drive disease progression in specific retinopathies including Stargardt disease (STGD), diabetic retinopathy (DR), light-induced retinopathy, and potentially age-related macular degeneration (AMD).[6, 7] Indeed, genetic ablation of essential enzymes[8, 9] and retinoid-binding proteins of the visual cycle,[10] or their inhibition,[11–16] protects the retina from degeneration induced by light.

In STGD and AMD, it is thought that the retinoid processing capability of the visual cycle may be overwhelmed as a consequence of prolonged exposure to light and/or attenuated metabolic state, hence allowing unbound RAL to form bisretinoids (e.g., A2E). The accumulation of bisretinoids in lipofuscin granules within the RPE[17] is believed to be detrimental for the retina,[18, 19] even though they may also represent photoreceptor detoxification products.[20] In the metabolically dysregulated diabetic eye, partial or total blockade of the visual cycle results in improvement of key markers of retinal stress likely due to modulation of photoreceptor activity.[7]

Central to the economy of the visual cycle is an enzyme known as RPE 65 kDa protein (RPE65) (Figure 1A).[5] To date, RPE65 is the only retinoid isomerase known to cleave and isomerize all-*trans*-retinyl esters (RE) to produce 11-*cis*-retinol (11cROL), the precursor of 11cRAL. RPE65 is an obligate component of the visual cycle, and thus it stands as a key target for pharmacological inhibition in visual cycle-associated diseases. *Rpe65* deficient mice are characterized by the absence of ocular 11-*cis*-retinoids resulting in dramatically impaired vision.[21, 22] Clinically, defects in the *Rpe65* gene are associated with blinding diseases resulting from the absence of 11cRAL in the retina.[23] As such, any effort to therapeutically inhibit RPE65 must avoid inducing diseases associated with visual chromophore deficiency. Thus, developing visual cycle inhibitors with ideal pharmacokinetic properties is crucial.

The first targeted pharmacological inhibitors of RPE65 were designed based on the hypothesis that the *trans* to *cis* isomerization reaction occurs through a carbocation intermediate (Supplemental Figure 1).[24] These inhibitors consisted of positively charged, amine-derivatives of retinol that mimic the transition-state of the retinoid isomerization reaction, with retinylamine being the most potent among them (Figure 1B).[11, 12] A concern that metabolites of retinylamine may activate the receptors of retinoic acid[25] together with the need to improve the solubility of these molecules prompted the development of inhibitors with a non-retinoid scaffold. Emixustat, first reported in 2012 by Acucela,[26–32] is the best characterized RPE65 inhibitor of this second class. This compound is ten times more potent than retinylamine *in vitro*.[33] It is orally bioavailable with good ocular

distribution[27] and selectively inhibits the visual cycle as demonstrated in phase I and II clinical trials.[34] In a phase III trial for AMD associated with geographic atrophy, emixustat therapy did not outperform the placebo control.[35]

Persistent suppression of RPE65 leads to problematic night-blindness (nyctalopia), and thus narrows the therapeutic window of emixustat. The γ-amino-α-aryl alcohol moiety of emixustat mediates crucial interactions with the residues Thr147 and Glu148 in the active site of RPE65 (Figure 1C),[33] but is also susceptible to rapid metabolism by a primary amine oxidase enzyme known as vascular adhesion protein 1 (VAP-1).[36] Consequently, the critical barriers to generating clinically effective RPE65 inhibitors lie in finely tuning the metabolic aspects of their pharmacokinetic profile. Previously we showed how selective fluorination of emixustat could be used to abrogate phase-I hydroxylation events.[15] Moreover, these studies partially addressed the metabolic liability of emixustat by deuterating the carbon alpha to the primary amine, but did not ablate it.

The work here aimed to comprehensively delineate the structural requirements of the γ-amino-α-aryl alcohol (what we have termed the RPE65 recognition element) to maintain high-affinity for RPE65 active site while circumventing VAP1-associated metabolic liability. We generated a library of 15 compounds (Figure 1D) to systematically test for RPE65 inhibition *in vitro*. The best inhibitors were tested *in vivo* by monitoring the kinetics of the visual cycle in response to a short period of bright light exposure. The most potent compound was subsequently tested for susceptibility to VAP-1 and cytochrome P-450 (CYP-450)-mediated clearance *in vitro* and its *in vivo* ocular distribution and serum levels were profiled. We also report detailed structural information on its complex with RPE65.

RESULTS:

Synthesis.

We organized our approach into four families of molecules. First, we aimed to investigate the geometric requirements of the γ-amino-α-alcohol recognition element with respect to the ether moiety. We were able to obtain all substituted (*ortho* and *para*) emixustat (here named **3a** for simplicity) via a previously reported synthetic pathway (Scheme 1).[15] Briefly, the commercially available phenols were reacted with potassium carbonate, (bromomethyl)cyclohexane, and DMF to give benzaldehydes **1a – c**. Subsequent aldol reaction between LDA and acetonitrile gave nitriles **2a – c** which were lastly reduced *via* LAH reduction to give amines **3a – c**.

Next, we shifted our focus to probe how perturbations to the γ-aminopropanol moiety would affect RPE65 recognition. The second subset of molecules would relocate the hydroxyl to a different position on the propylene chain while at the same time conserving the amine moiety on the chain. A novel approach (Scheme 2) was employed to synthesize these three additional amino alcohols. Anhydrous HCl gas (generated *in situ*) was bubbled through a suspension of commercially available tyrosine derivatives in methanol. Subsequent Boc protection afforded the N-Boc protected methyl esters **4a – c**. Phenols **4a – c** were deprotonated to undergo S_N2 displacement of (bromomethyl)cyclohexane to give esters **5a –**

c. Finally, consecutive ester reduction with LAH and Boc deprotection using trifluoroacetic acid gave target aminopropan-1-ols **6a - c**.

A third subfamily of molecules were synthesized that all possess a truncated aliphatic chain compared to emixustat. Amine **11a** was synthesized following a previously reported method.[24] Three amines were synthesized using a general method illustrated in Scheme 3. In short, benzaldehyde **1a** or acetophenone **7** were reduced with sodium borohydride to give the corresponding benzylic alcohols **8a – b**. These benzylic alcohols were converted to the analogous benzylic nitriles in two steps: first by reaction of alcohols with phosphorus tribromide then substitution with potassium cyanide to give benzylic nitriles **9a – b**. Final nitrile reduction using borane yielded the desired short chain derivatives **11b – c**. Finally, the fluorinated version of **11b** was synthesized. We employed a Henry reaction between benzaldehyde **1e**, nitromethane, and ammonium acetate to give the unsaturated nitro compound **10**. Simultaneous olefin and nitro reduction was achieved by addition of LAH under heat to give truncated amine **11d**.

Lastly, we aimed to synthesize methylated derivatives of emixustat to maximize the structural correspondence between **3a** and the retinoid backbone. First, amine **16a** was synthesized according to literature precedent.[24] In short, Sonogashira coupling of 2-(prop-2-yn-1)isoindoline-1,3-dione with aryl iodide **12** gave alkyne **13**. Consecutive hydrogenation of the alkyne then phthalimide deprotection with hydrazine gave propylamine **16a**. As displayed in Scheme 4, novel synthetic pathways were taken to synthesize **16b – 16e**. We started with a Horner-Wadsworth-Emmons condensation between either acetophenone **7,** benzaldehydes **1a** or **1e** and, with the appropriate phosphonates, the reaction afforded unsaturated nitriles **14 – 15a/b**. Subsequent addition of LAH simultaneously reduced both the alkene and nitrile to give target amines **16b** and **16c,** respectively, and hydrogenation of nitrile **15b** gave the desired fluorinated molecule **16d**. Finally, methylamine **16e** was readily made in two steps starting with the selective mesylation of diol MB-002[13] followed by displacement with methylamine in a sealed tube.

RPE65 inhibitory properties of tested compounds.

A total of 15 derivatives were tested for their inhibitory effects on RPE65 *in vitro* by monitoring their impact on 11-*cis*-retinol production by bovine RPE microsomes using established assay conditions (Table 1). First, because almost all studied emixustat derivatives to date have the γ-amino-α-aryl alcohol moiety *meta* relative to the 6 membered ring,[13–15] we assessed the effect of phenyl ring substitution pattern on RPE65 inhibition (Figure 2A). Emixustat (**3a**) had a half-maximal inhibitory concentration (IC_{50}) of 200 ± 20 nM, consistent with published data[15], whereas **3b** (*para*) and **3c** (*ortho*) analogs exhibited substantially higher IC_{50} values (8.08 ± 3.44 μM and 4.67 ± 1.45 μM, respectively) suggesting that the bent geometry imparted through the *meta* configuration of emixustat is ideally complementary to the RPE65 active site, supporting our overall hypothesis that the most effective RPE65 inhibitors are isosteres of the 11-*cis*-retinyl cation transition state. Next, we tested the effect of swapping the position of the primary amine with the alcohol in the γ-amino-α-aryl alcohol moiety (Supplemental Figure 2A). Compounds **6a – c** showed no inhibition of RPE65 within the concentration range of 0.1-50 μM. The lack of inhibitory

activity observed for **6a** was particularly striking given the known tolerance of alcohol substitution at the γ position. This outcome may be due to relatively poor stabilization of the amine functionality within the RPE65 active site, which is predicted to be protonated in our assay conditions, in the γ position as compared to the α position. Interestingly, the lack of dose-response relationship observed for amine **6c** also suggests that compounds in this family have no added potency enhancement by being in the *para* configuration.

Next, we investigated the series of emixustat derivatives with truncated γ-amino-α-aryl alcohol (Figure 2B). We hypothesized that this modification may impact inhibitory activity by increasing or decreasing the distance between the primary amine of the inhibitor and Glu148 and palmitoyl-associated carboxylate moieties (Figure 1C). Compounds **11a-d** were tested in the concentration range of 0.02 - 20 μM. Amine **11a** was substantially less potent than **3a** ($IC_{50} = 3.19 \pm 0.81$ μM) suggesting that the proper positioning of the cationic amine is crucial for optimal active site interaction. With this observation we sought to probe the 2-amino-1-hydroxyethane chain of amine **11a** to determine if further modifications would affect inhibitory potency. Removal of the hydroxyl moiety gave **11b** ($IC_{50} = 420 \pm 110$ nM), a compound with 7.6-times more potent activity towards RPE65 relative to amine **11a**. Substitution of the alcohol with a methyl group yielded **11c**, with weaker inhibition ($IC_{50} = 6.73 \pm 0.26$ μM) likely arising from non-favorable interactions with the Thr147 hydroxyl moiety. This result was somewhat unexpected as one of the hypotheses we sought to test throughout the series described here was whether a mimic of the retinoid C20 methyl group would impart enhanced activity. Instead, it resulted in low RPE65 inhibition, suggesting that this molecule cannot occupy RPE65's active site like the retinyl cation does (Supplemental Figure 1). Fluorinated compound **11d** ($IC_{50} = 1.23 \pm 0.13$ μM) notably showed a three-fold decrease in RPE65 inhibition relative to **11b.** This result was incongruent with our previous findings that aryl fluorination at this position should impart higher affinity towards RPE65.[15] These results together suggest that **11b** and **11d** do not occupy the same binding position as emixustat relative to the iron center of RPE65. Also, these data indicate that, at least *in vitro,* the hydroxyl group of the γ-amino-α-aryl alcohol moiety is not obligatory for RPE65 inhibition.

Next, we applied the same logical considerations of **11a-d** to the γ-amino-α-aryl alcohol recognition element. Specifically, we tested the regiospecific incorporation of a methyl group to generate compounds **16a-d**. These compounds were tested in the concentration range between 0.02-10 μM. Plotted in Figure 2C, amine **16a** ($IC_{50} = 1.55 \pm 0.30$ μM) and **16b** ($IC_{50} = 820 \pm 150$ nM), showed decreased activity towards RPE65 relative to **3a** with an eight-fold and four-fold decrease in inhibition of RPE65 respectively. These results indicate that the addition of only a methylene unit compared to **11b** decreases RPE65 inhibition, suggesting the critical nature of proper placement of the amino group. Again, in aiming to mimic the retinoid C20 methyl group (as with **11b** and **11c**) we found that methylation at the α and β-carbons (**16b and 16c, respectively**) roughly doubled and quadrupled potency relative to **16a**. The enhanced potency of **16c** relative to **16b** may arise from the more ideal structural correspondence between the β-methyl and retinoid C20 methyl groups (Supplemental Figure 1). It is important to note that **16c** achieves this level of potency without the α-hydroxyl moiety found in emixustat. Again, using the rationale as above we

generated a fluorinated derivative of **16c** (**16d**) but it was inactive (Supplemental Figure 2B). Collectively, these results demonstrate that a γ-amino-β-methyl moiety is sufficient to attain significant RPE65 inhibition *in vitro.* However, they also highlight the critical spacing and composition of the γ-amino-α-aryl alcohol recognition element of **3a** with RPE65 (Figure 1C).

Lastly, we explored the effect of methylating the primary amine of **3a** on RPE65 inhibition. We were initially surprised that amine **16e** (IC_{50} = 290 ± 50 nM) retains most of the activity of emixustat, as our prediction was that the N-methyl functionality would significantly obstruct the crucial interaction of the ammonium as described in our previous structure of emixustat with RPE65.[33] Nevertheless, this was a crucial result as it showed that amine methylation does not prevent potent inhibition of RPE65 *in vitro.*

Inhibition of RPE65 *in vivo*

Next, we tested the effect of the most potent compounds (**11b** and **16b-e**) on visual cycle function in BALB/cJ mice. Figure 3A illustrates the experimental procedure used in this study. Figure 3B (left panel) shows representative chromatograms obtained from animals four hours after treatment with **3a** (blue trace), **16e** (purple trace) and DMSO (green trace). Compared to the dark adapted (DA) (black trace) and the vehicle-treated chromatograms, both **3a** and **16e** groups showed large accumulation of RE accompanied by significantly reducing recovery of 11cRAL. Peaks corresponding to 11cRAL and RE were identified by retention time and UV-Vis absorption spectrum (Figure 3B, **insert**). Figure 3B, right panel, shows representative chromatograms obtained from the same groups but 24 hours after treatment with **3a** (blue trace), **16e** (purple trace) and DMSO (green trace). One day after injection, 11cRAL and RE levels were not yet recovered in the groups treated with **3a** and **16e**.

The quantification of 11cRAL and RE for each group is summarized in Table 2. Baseline levels of 11cRAL (Figure 3C, black bar) and RE (Figure 3D, black bar) were established in dark adapted (DA) animals were 384.1±15.2 pmol/eye and 67.4 ± 12.4 pmol/eye respectively. In the groups treated with vehicle (Figure 3C–D, green bars) and **16d** (Figure 3C–D, grey bars), four hours of dark adaptation were sufficient to restore baseline levels of both 11cRAL and RE, 389.5 ± 17.2 and 58.2 ± 11.0, in the vehicle group, respectively; 398.0 ± 26.6 pmol/eye and 122.7 ± 30.6 pmol/eye in the **16d** group, respectively.

By contrast, 24 hours post treatment with **3a** (Figure 3C–D, blue bars), the level of 11cRAL were significantly lower compared to the DA group and vehicle groups, 137.4 ± 44.5 pmol/eye, which corresponds to 36% of the DA level. Consistent with suppressed11cRAL synthesis, RE levels were significantly increased compared to DA group at 377.3 ± 54.5 pmol/eye. This result corroborated the inhibition of RPE65 activity we observed in bovine RPE microsomes (Figure 2A) and demonstrated strong RPE65 inhibition *in vivo* as reported previously.[13] Treatment with **16e** (Figure 3C–D, purple bars) also showed potent RPE65 inhibition, consistent with *in vitro* measurements. 24 hours after administration of **16e**, 11cRAL and RE levels were 201.8 ± 53.2 pmol/eye and 215.4 ± 99.2 pmol/eye, respectively.

Notably, the concentration of 11cRAL per eye was 53% of the DA. This result suggested that mono-methylation of the emixustat did not alter the ocular targeting.

Treatment with compound **11b** (Figure 3C–D, red bars) did not display hallmarks of inhibited RPE65 activity *in vivo*. Both 11cRAL and RE levels were completely recovered four hours after exposure to light, 393.2 ± 18.2 pmol/eye and 89.5 ± 5.2 pmol/eye for **11b,** respectively. This result differed from our measurements of RPE65 inhibition *in vitro* (Figure 2B) indicating that **11b** did not accumulate sufficiently in the RPE *in vivo*. Thus, truncation of γ-amino-α-aryl alcohol moiety together with removal of the alcohol are not viable strategies for the inhibition of RPE65 *in vivo*.

Compounds, **16c** (Figure 3C–D, yellow bars) and **16b** (Figure 3C–D, orange bars) showed minor RPE65 inhibition four hours after treatment, but animals were fully dark adapted after 24 hours. 11cRAL and RE levels were 370.5 ± 9.1 pmol/eye and 123.9 ± 36.4 pmol/eye for **16c**, respectively; 253.5 ± 9.0 pmol/eye and 85.6 ± 12.7 pmol/eye for **16b**, respectively. We note that the visual cycle inhibition observed for **16b** may be due to non-specific toxicity as all animals showed impaired body movement even 24 hours after treatment.

To summarize, all tested compounds that failed to inhibit RPE65 *in vivo* were primary amines without an alcohol. By contrast, the inhibition profile of the secondary amine **16e** resembled that of emixustat. Taken together these results demonstrated that both the amine and alcohol of the γ-amino-α-aryl alcohol moiety are required to attain sustained RPE65 inhibition *in vivo*.

Pharmacokinetics of compound 16e

Next, we investigated the stability of **16e** to oxidative metabolism *in vitro* with an HPLC-based activity assay using mouse aorta homogenates as the source of VAP-1 enzyme. Previous investigations highlighted that elimination of emixustat *in vivo* is prominently driven by VAP-1 present in the vasculature. *In vitro* experiments identified ACU-5201 aldehyde as the major emixustat product of VAP-1 catalytic activity (Figure 4A).[15, 36] Because VAP-1 exerts oxidative deamination selectively towards primary amines,[37] the secondary amine of compound **16e** would be predicted to be insensitive to VAP-1 enzymatic activity. We tested this hypothesis by comparing the rate of oxidative deamination of **3a** versus that of compound **16e**.

The formation of the dehydrated aldehyde product (ACU-5201) was monitored by reverse-phase HPLC (Figure 4B–C) by comparison of its retention time and UV-vis spectra to that of the authentic synthetic standard ACU-5201 (Figure 4D) (synthesis of ACU-5201 reported previously by us[15]). Quantitative analysis is illustrated in Figure 4E and numerical results are summarized in Table 3.

As expected, **3a** was rapidly metabolized by VAP-1. After 1 hour of incubation, 18% of emixustat was metabolized to ACU-5201, which increased to 50% after four hours, similar to our previous findings.[15] By contrast, mono-methylation of the γ-amino-α-aryl alcohol moiety (compound **16e**) reduced the formation of ACU-5201 by about 99.5% after one hour and 96.25% after four hours.

We next studied whether **16e** is a prodrug of **3a**, as demethylation of the secondary amine by enzymes of the CYP-450 family would generate **3a** (Figure 5A) which is a strong RPE65 inhibitor *per se* (Figure 3B–C, Table 2). To test this possibility, we investigated the metabolism of compound **16e** *in vitro* with an HPLC-based activity assay using mouse liver homogenates as the source of CYP-450 enzymes. Compounds **16e** or **3a** were added at different concentration (0.15 - 200 μM) to a fixed amount of mouse liver microsomes and the kinetics of the reactions were followed at time points ranging from zero to one hour (Figure 5B–C). This assay was validated by a negative control reaction in which the NAPDH cofactor required for CYP-450 activity was omitted (Supplemental Figure 3A). The numerical results from this experiment are summarized in Table 4.

One-hour exposure of 200 μM **16e** to liver microsomes (purple trace) elicited a minor amount of demethylation as demonstrated by the presence of the peak corresponding to **3a** when compared to the chromatogram of the reaction run with **3a** (blue trace). However, *in vitro* this metabolic pathway accounted for a small amount of the clearance of **16e.** We observed the rapid appearance of another metabolite of **16e** which eluted earlier compared to **16e** (Supplemental Figure 3B), indicative of a higher hydrophilicity compared to that of the parent compound **16e**. However, this metabolite was not readily amenable to precise chemical identification by mass spectrometry. Notably, this metabolite of **16e** was not observed for emixustat, indicating that mono-methylation of the primary amine in the RPE65 recognition motif conferred susceptibility to a new elimination pathway. Additionally, we did observe the formation of ACU-5201 from emixustat in this mouse liver microsome assay (Supplemental Figure 3B, orange trace), indicating that the liver may also play a role in the oxidative deamination of this molecule in addition to the general vasculature[36, 38] although ACU-5201 was observed only in trace amount.

Our microsomal metabolism data allowed us to determine the intrinsic clearances (C_{int}) of **16e** and **3a**. We derived the initial velocity (V_0) values at substrate concentrations in the range of 0.15 - 200 μM (**Supplemental Figure 5 C-E**) and fit these data with the Michaelis-Menten equation to derive steady-state kinetic constants and intrinsic clearance (V_{max}/K_m) values (Table 5). As shown in Figure 5C, **16e** is characterized by a higher V_{max} compared to **3a**, 70.85 pmol/min and 119.5 pmol/min respectively, hence indicating that in the liver **16e** was metabolized at a 1.7 times faster rate than **3a**. This finding was consistent with a larger K_m for **3a** compared to **16e**, 126.3 pmol/mL and 39.01 pmol/mL. Finally, the C_{int} of **16e** was 1.83 L/hour/mg while that of **3a** was 0.34 L/hour/mg. Thus, the methylation of the primary amine in the RPE65 recognition motif of emixustat imparted a 5.5 times higher hepatic clearance of **16e** as compared to **3a**.

This result raised the question about the extent to which this minor *in vitro* conversion of **16e** to **3a** was relevant *in vivo*. To answer this question, we followed the progress of **16e** elimination in the mouse eye and serum after a single IP injection of **16e** in DMSO (50 μL, 10 mg/kg). In this experiment samples were collected at one, four and 24 hours post-administration. We also included two control groups, animals treated with a single IP injection of **3a** in DMSO (50 μL, 10 mg/kg) or vehicle alone (50 μL, DMSO). The collection

of the sample from the control groups was limited to one hour after IP injection. Numerical results from these experiments are summarized in Table 6.

One hour after injection, **16e** was found in eye (Figure 5D, purple bars) and in plasma (Figure 5E, purple bars) extracts, thus confirming the distribution of this visual cycle modulator in the ocular tissue. **16e** levels decreased significantly at four hours and approached baseline levels in both eye and plasma at 24 hours after injection, suggesting elimination of **16e** from these compartments. In the same animals, **3a** (blue bars) was quantifiable at all the time points that we investigated. This result demonstrated **16e** demethylation *in vivo,* but its RPE65 inhibition was not representative of **16e** being a pro-drug of **3a,** most clearly illustrated by the four hour timepoint where **16e** was still present at significant concentrations in the eye. Figure 5D–E also illustrates the most problematic pharmacokinetic property of **3a**/emixustat, namely that this molecule will persist in ocular tissues for long time periods, leading to the main side effect noted in clinical trials, nyctalopia. Although we found that the conversion to **3a** was significant, as illustrated by the relative concentrations at the four hour time point, what was converted to **3a** persisted for only 24 hours. In contrast, in a previous study,[15] we showed that IP injection of an equivalent dose of **3a** led to a persistence of significant **3a** concentrations in the eye for up to seven days post injection. Hence, the almost absent levels of **3a** in mouse eyes 24 hours after **16e** administration were indicative of shorter duration of action of this compound compared to **3a**. All together, these results demonstrate that compound **16e**, besides being a potent RPE65 inhibitor, was also resistant to VAP-1 oxidative deamination. However, VAP-1 resistance came at the cost of increased hepatic metabolism and minor conversion to **3a**. resistant to VAP-1 oxidative deamination. However, VAP-1 resistance came at the cost of increased hepatic metabolism and minor conversion to **3a**.

Crystal structure of RPE65 in complex with 16e

To gain an understanding of how **16e** can be accommodated within the RPE65 active site cavity, we determined the crystal structure of RPE65 in complex with **16e** in space group $P6_522$ to a nominal resolution of 2.1 Å (Figure 6A, Table 7). The data showed clear evidence for binding of **16e** and a palmitate ligand in the proximal and distal regions of the RPE65 active site, respectively (Figure 6B), similar to the modes of binding observed in other RPE65-ligand complexes (Supplemental Figure 4A). The terminal methyl group was observed to point toward the palmitate carboxylate carbon atom with a C-C interaction distance of ~3 Å (Supplemental Figure 4B). To confirm the methyl group positioning, we deleted that region of the model, performed 10 cycles of restrained refinement, and then inspected the resulting difference map. Consistent with our initial interpretation, we observed a strong difference map peak at the position of the deleted methyl group that remained despite shifts in the ligands that were made by the refinement program in an attempt to quench the difference map peak (Supplemental Figure Figure 4C). Comparison of our final refined RPE65-**16e** complex with a previously reported RPE65-emixustat complex in the same space group (PDB accession code: 4RYX) revealed a similar mode of inhibitor binding indicating that the terminal methyl group is readily accommodated within the RPE65 active site (Supplemental Figure 4C).

DISCUSSION/CONCLUSION:

The results of this study address three important aspects of targeted RPE65 inhibition. First, we have comprehensively defined *in vitro* and *in vivo* structure-activity relationships of the γ-amino-α-aryl alcohol recognition element of emixustat, a region of the molecule we have argued is critical for RPE65 active site recognition. Second, we have identified a key modification to the emixustat molecule that largely abrogates a major phase 1 metabolic pathway for emixustat elimination that is mediated by VAP-1 amine oxidase, though enhancing overall hepatic intrinsic clearance. Third, we have demonstrated with **16e** that the key pharmacophore for RPE65 can be expanded to include modifications of the amine-portion of the recognition element. Together, these data provide a capstone to our efforts to tune the PD/PK properties of emixustat to achieve a more therapeutically viable molecule. Indeed, emixustat-induced RPE65 inhibition is extremely long-lived due to ocular accumulation, a property that complicates the posology of emixustat. The faster metabolism of **16e** *in vitro* and *in vivo* is possibly due in part to the increased hydrophobicity this compound as compared to emixustat. Therefore, our results establish a new strategy to control the duration of action of visual cycle modulators based on emixustat scaffold. Primary amine visual cycle modulators have been proposed to exert protective effects against light-induced retinal damage through two distinct mechanisms: 1) suppression of visual cycle kinetics through direct inhibition of RPE65 and 2) sequestration of reactive retinaldehyde through Schiff base formation. Because **16e** is a secondary amine, Schiff base formation is expected to be less efficient compared to primary amine compounds. Therefore, we expect any protective effect exerted by **16e** would occur through a direct visual cycle suppression mechanism. Likewise, we also expect that the secondary amine of 16e will reduce or exclude its susceptibility to LRAT-mediated amidation, which is proposed to be responsible for the long duration of action of retinylamine[39] and emixustat.[13] In the future, the complete elucidation of **16e**'s pharmacological effects on the physiology of vision will establish if this compound holds translational potential for the treatment of retinopathies.

In a previous publication, we proposed a strategy for elimination of the hydroxylation components of metabolism through the strategic incorporation of fluorine.[15] Here, we explored the structural requirements of what we have termed the RPE65 recognition element. Given the hypothesis that effective inhibition of RPE65 is most easily achieved via an amine-containing molecule to mimic the carbocation transition state of the retinoid isomerization reaction, better strategies were needed to address the metabolic liability of the primary amine of emixustat. The metabolism of primary amine drugs by VAP-1 is a lesser known phase I pathway,[40] but has nevertheless been shown important for a number of primary amine-containing drugs besides emixustat[36] including primaquine[41] and tresperimus.[42] Previously, we argued that deuteration at the α-position to the amine could attenuate VAP-1 oxidation,[15] but here we present an effective strategy by way of generating a secondary amine that almost completely abrogates VAP-1 activity. While the VAP-1 results were in line with defined substrate requirements, the potent nature of **16e** was unexpected. Based on our previous structures of RPE65, we would have predicted that the additional methyl group of **16e** would interfere with critical interactions with the iron center. Another important result of the studies described here are the inhibition results seen

with compounds **6a** and **6b**. When considering previous inhibition data of MB-002,[13] we predicted a level of flexibility at the position α to the aryl moiety. Given that **6a** and **6b** showed no inhibition *in vitro*, we can now define this position as critical to the recognition element. It is likely that **6a** and **6b** are protonated at physiological pH values and enter the RPE65 active site in an ionized form. Assuming this is the case, we speculate that the positively charged amine group is poorly stabilized in the γ and β positions relative to the α position, which is predicted to reside in a region of high electronegativity arising from palmitate and Glu148 carboxylate moieties. This lack of electrostatic complementarity could explain the lack of RPE65 inhibitory activity of **6a** and **6b**. Interestingly, a recent study by Wang *et al.*[43] demonstrated that sulfoximine substitution for the alcohol group of emixustat also yields a potent inhibitor, indicating that other neutral hydrogen bond donors are tolerated at this position.

In light of the analysis above, methylated derivatives of γ-amino-α aryl alcohol chain generally matched with prediction. The α-methyl derivatives **11c** and **16b** displayed the lowest level of inhibition, likely due to the loss of the Thr147 hydrogen bond. Integration of a β-methyl group afforded promising compound **16c.** Had this lead molecule displayed more promising *in vivo* properties it would have represented a new direction in the development of RPE65 inhibitors, specifically, molecules that mimic the C20 retinoid methyl group. Moving forward, the clear vertical progress we report here is twofold. First, we have shown how secondary amines can be accommodated into the RPE65 binding pocket and afford a new family of inhibitors that are metabolically stable to VAP-1. Second, we defined the importance of the α-aryl hydrogen bond acceptor in RPE65 inhibition.

Most of the molecules in this work were synthesized using novel routes. Facile functional group manipulation of commercially available tyrosine derivatives led ultimately to the γ-aryl propanols **6a-c**. This subtle protection strategy bypasses the potentially problematic selective installation of amino moiety to the γ or β-position of the propanol chain. The syntheses of **11d** and **16b-d** demonstrate generation of the primary amine moiety by the simultaneous reduction of unsaturated nitro/cyano molecules. This strategy is comparable in length to the known aldol and Mannich-type routes employed to synthesize derivatives of emixustat.[13–15, 33] We believe the synthetic strategies displayed in this work are efficient, yet high yielding, and can be powerful general approaches for medicinal chemists interested in primary-amine containing drug scaffolds.

EXPERIMENTAL SECTION:

General Synthetic Methods.

All reactions were performed in oven-dried glassware under inert atmosphere. Diisopropylamine was fractionally distilled in CaH_2 prior to use. All reagents were purchased from various vendors (Sigma-Aldrich, Fisher, Oakwood, Combi Blocks, and AA Blocks) were used as supplied without purification. Thin-layer chromatography (TLC) was performed on 0.25 mm glass-backed EMD Millipore 60 F254 plates. Visualization of TLC plates was accomplished with UV light (254 nm) and final amines were stained with permanganate ($KMnO_4$). Purification of all intermediates was achieved by use of the CombiFlash Nextgen 100 (Teledyne Isco). All final target amines were purified manually by

forced air-flow on silica gel (Merck, 230 – 400 mesh) using eluting solvents (reported as V/V ratio mixture), and finally filtered through sodium sulfate after solvents were removed by rotary evaporation. The ^{1}H, ^{13}C, ^{19}F NMR nuclear magnetic resonance (NMR) spectra were recorded at 25 °C on Bruker AVANCE NMR spectrometer operating at 500 MHz. ^{19}F NMR spectra were recorded without decoupling from protons. Chemical shifts were reported in δ units, part per million, with reference to the residual solvent peak CDCl$_3$ (δ 7.26) and DMSO-d_6 (δ 2.50) for ^{1}H and CDCl$_3$ (δ 77.3) and DMSO-d_6 (δ 39.5) for ^{13}C NMR spectra. NMR data are presented in the following order: chemical shift, peak multiplicity (s = singlet, d = doublet, t = triplet, q = quartet, m = multiplet, dd = doublet of doublet, dt = doublet of triplet, ddd = doublet of doublet of doublet, dq = doublet of quartet), coupling constant (in Hz). Analytical HPLC analysis of final targets was carried out on an Agilent 1260 series system consisting of a G4204A quaternary pump, a G4226A ALS auto-sampler, and a G1316C column compartment. The separation was performed on a Shimadzu Premier C18 (5 μm, 100 mm × 4.5mm) column using a mobile phase consisting of 0.1% formic acid in water (A) and 0.1% formic acid in acetonitrile (B) at a flow rate of 1 mL/min, and the mobile-phase gradients and time course were as follows: 0 – 5 min, 95% A/5% B; 5 – 10 min, 95–5% A/5–95% B; 10 – 20 min, 5% A/95% B; 20 – 25 min, 5-95% A/95-5% B; 25 – 30 min, 95% A/5% B. The final biologically tested compounds displayed 95% purity except for **11d** and **16b** (>90%). Synthesis of the target emixustat amines is detailed below, while the synthesis of all the precursors, NMR spectra for all compounds, and HPLC traces of final targets are described in the supporting information.

3-Amino-1-(4-(cyclohexylmethoxy)phenyl)propan-1-ol (3b). General Procedure
1.—Compound **2b** (300 mg, 1.2 mmol) in THF (1 mL) was added dropwise to an ice-cold stirred solution of lithium aluminum hydride (175 mg, 4.6 mmol) in THF (4 mL) under argon. The resulting mixture stirred at 0 °C for 1 h then was slowly quenched by the dropwise addition of water (300 μL), 15% NaOH (300 μL), and water (900 μL) consecutively. The reaction mixture was allowed to stir at room temperature (rt) for 0.5 h, filtered through cotton, diluted with water (30 mL), extracted with dichloromethane (2 × 10 mL), dried over sodium sulfate, and filtered. Following concentration in vacuo, the crude product was then purified by flash column chromatography giving a tan solid (144 mg, 47%). HPLC: t_R = 10.0 min (95%). ^{1}H NMR (500 MHz, CDCl$_3$) δ 7.28 (d, J = 8.7 Hz, 2H), 6.86 (d, J = 8.7 Hz, 2H), 4.90 (dd, J = 8.7, 3.3 Hz, 1H), 3.74 (d, J = 6.4 Hz, 2H), 3.10 (ddd, J = 12.5, 5.7, 4.2 Hz, 1H), 2.94 (ddd, J = 12.7, 9.2, 3.9 Hz, 1H), 1.91 – 1.65 (m, 9H), 1.35 – 1.14 (m, 4H), 1.04 (qd, J = 12.2, 3.4 Hz, 2H). ^{13}C NMR (126 MHz, CDCl$_3$) δ 158.1, 137.1, 126.9, 114.4, 75.3, 73.6, 40.7, 39.9, 37.8, 30.0, 26.6, 25.9. HRMS (ESI+): (m/z) calculated for C$_{16}$H$_{26}$NO$_2$ [M+H]$^+$ 264.1958; found 264.1957.

3-Amino-1-(2-(cyclohexylmethoxy)phenyl)propan-1-ol (3c).—General procedure 1
was followed using nitrile **2c** (660 mg, 2.54 mmol) to give a yellow solid (294 mg, 44%). HPLC: t_R = 9.8 min (97%). HPLC: t_R = 9.630 min (97%). ^{1}H NMR (500 MHz, CDCl$_3$) δ 7.50 (dd, J = 7.5, 1.8 Hz, 1H), 7.20 (td, J = 7.7, 1.8 Hz, 1H), 6.96 (td, J = 7.5, 1.1 Hz, 1H), 6.82 (dd, J = 8.3, 1.1 Hz, 1H), 5.23 (dd, J = 8.0, 3.5 Hz, 1H), 3.77 (qd, J = 9.0, 6.0 Hz, 2H), 3.04 – 2.98 (m, 1H), 2.97 – 2.91 (m, 1H), 2.51 (s, 2H), 2.03 – 1.91 (m, 1H), 1.90 – 1.67 (m, 8H), 1.36 – 1.16 (m, 4H), 1.15 – 1.03 (m, 2H). ^{13}C NMR (126 MHz, CDCl$_3$) δ 155.6,

133.2, 127.8, 126.6, 120.5, 110.9, 73.3, 70.5, 40.5, 38.4, 37.9, 30.1, 30.1, 26.6, 26.0. HRMS (ESI+): (m/z) calculated for $C_{16}H_{26}NO_2$ [M+H]$^+$ 264.1958; found 264.1957.

3-Amino-3-(3-(cyclohexylmethoxy)phenyl)propan-1-ol (6a). General Procedure 2.

—Compound **5a** (300 mg, 0.76 mmol) in THF (1 mL) was added dropwise to an ice-cold stirred solution of lithium aluminum hydride (175 mg, 4.6 mmol) in THF (4 mL) under argon. The resulting mixture stirred at 0 °C for 1 h then was slowly quenched by the dropwise addition of water (300 μL), 15% NaOH (300 μL), and water (900 μL) consecutively. The reaction mixture was allowed to stir at rt for 0.5 h, filtered through cotton, diluted with water (30 mL), extracted with dichloromethane (2 × 10 mL), and dried over sodium sulfate. Following filtration, solvents were removed in-vacuo to give a colorless syrup (140 mg). This solid was dissolved in DCM (5 mL) and TFA (0.6 mL, 7.83 mmol) was added and stirred for 1 h at room temperature. The solution was basified with 15% NaOH (20 mL) and extracted with DCM (2 × 10 mL). The combined layers were dried over Na_2SO_4, concentrated under reduced pressure, and purified by flash column chromatography to finally give a colorless syrup (57 mg, 28%). HPLC: t_R = 9.8 min (95%). ^{1}H NMR (500 MHz, CDCl$_3$) δ 7.24 (t, J = 7.8 Hz, 1H), 6.89 – 6.84 (m, 2H), 6.81 (dd, J = 7.6, 2.0 Hz, 1H), 4.17 (dd, J = 9.6, 3.6 Hz, 1H), 3.87 – 3.77 (m, 2H), 3.73 (d, J = 6.4 Hz, 2H), 3.35 (s, 3H), 2.08 – 1.97 (m, 1H), 1.93 – 1.82 (m, 3H), 1.81 – 1.66 (m, 4H), 1.34 – 1.16 (m, 3H), 1.04 (qd, J = 12.3, 3.4 Hz, 2H). ^{13}C NMR (126 MHz, CDCl$_3$) δ 159.9, 130.1, 118.1, 113.9, 112.4, 73.6, 61.8, 56.7, 38.0, 37.8, 30.0, 26.6, 25.9. HRMS (ESI): (m/z) calculated for $C_{16}H_{26}NO_2$ [M+H]$^+$ 264.1964; found 264.1957.

2-Amino-3-(3-(cyclohexylmethoxy)phenyl)propan-1-ol (6b).

—The general procedure 2 was applied to compound **5b** (250 mg, 0.63 mmol) giving a colorless syrup (56 mg, 27%). HPLC: t_R = 9.9 min (97%). ^{1}H NMR (500 MHz, CDCl$_3$) δ 7.20 (t, J = 7.8 Hz, 1H), 6.78 – 6.71 (m, 3H), 3.74 (d, J = 6.4 Hz, 2H), 3.64 (dd, J = 10.5, 4.0 Hz, 1H), 3.37 (dd, J = 10.5, 7.2 Hz, 1H), 3.17 – 3.08 (m, 1H), 2.76 (dd, J = 13.4, 5.2 Hz, 1H), 2.49 (dd, J = 13.4, 8.7 Hz, 1H), 1.91 – 1.84 (m, 2H), 1.80 – 1.67 (m, 5H), 1.58 (s, 3H), 1.35 – 1.16 (m, 4H), 1.05 (qd, J = 12.2, 3.4 Hz, 2H). ^{13}C NMR (126 MHz, CDCl$_3$) δ 159.7, 140.3, 129.6, 121.4, 115.6, 112.4, 73.5, 66.7, 54.2, 41.3, 37.9, 30.0, 26.6, 25.9. HRMS (ESI): (m/z) calculated for $C_{16}H_{26}NO_2$ [M+H]$^+$ 264.1964; found 264.1958.

2-Amino-3-(4-(cyclohexylmethoxy)phenyl)propan-1-ol (6c).

—Following the general procedure 2, reduction then deprotection of **5c** (300 mg, 0.77 mmol) afforded a white solid (75 mg, 37%). HPLC: t_R = 9.9 min (99%). ^{1}H NMR (500 MHz, CDCl$_3$) δ 7.08 (d, J = 8.5 Hz, 2H), 6.84 (d, J = 8.5 Hz, 2H), 3.73 (d, J = 6.3 Hz, 2H), 3.64 (dd, J = 10.7, 3.9 Hz, 1H), 3.37 (dd, J = 10.6, 7.2 Hz, 1H), 3.11 (s, 1H), 2.73 (dd, J = 13.7, 5.3 Hz, 1H), 2.48 (dd, J = 13.6, 8.5 Hz, 1H), 1.87 (d, J = 14.7 Hz, 2H), 1.76 (d, J = 12.5 Hz, 4H), 1.25 (d, J = 89.0 Hz, 4H), 1.04 (qd, J = 12.3, 3.4 Hz, 2H). ^{13}C NMR (126 MHz, CDCl$_3$) δ 158.1, 130.3, 130.2, 114.7, 73.7, 66.5, 54.4, 40.1, 37.8, 30.0, 26.6, 25.9. HRMS (ESI): (m/z) calculated for $C_{16}H_{26}NO_2$ [M+H]$^+$ 264.1964; found 264.1961.

2-(3-(Cyclohexylmethoxy)phenyl)ethan-1-amine (11b).

—Nitrile **9a** (2.0 g, 8.7 mmol) and borane dimethyl sulfide complex (5M in ether, 5.3 mL, 26.5 mmol) in THF

(40 mL) was stirred at reflux for 4 h under argon. The resulting mixture was cooled in an ice-bath and quenched with MeOH until no bubbling was observed. Solvents were removed by rotary evaporation and residue was diluted in water (30 mL) and extracted with DCM (3×10 mL). The combined organic layers were dried over sodium sulfate and solvents removed under reduced pressure. Crude material was purified by flash column chromatography to finally give a colorless syrup (133 mg, 5%). HPLC: $t_R = 10.0$ min (99%). ^{1}H NMR (500 MHz, CDCl$_3$) δ 7.20 (dd, $J = 9.0, 7.5$ Hz, 1H), 6.84 – 6.67 (m, 3H), 3.74 (d, $J = 6.4$ Hz, 2H), 2.97 (t, $J = 6.8$ Hz, 2H), 2.72 (t, $J = 6.8$ Hz, 2H), 1.91 – 1.83 (m, 2H), 1.82 – 1.65 (m, 4H), 1.45 (s, 4H), 1.34 – 1.17 (m, 3H), 1.05 (qd, $J = 12.3, 3.4$ Hz, 2H). ^{13}C NMR (126 MHz, CDCl$_3$) δ 159.6, 141.5, 129.5, 121.1, 115.3, 112.1, 73.5, 43.6, 40.3, 37.8, 30.0, 26.6, 25.9. HRMS (EI): (m/z) calculated for C$_{16}$H$_{26}$NO$_2$ [M+H]$^+$ 233.1780; found 233.1779.

2-(3-(Cyclohexylmethoxy)phenyl)propan-1-amine (11c).—Borane dimethylsulfide complex (5.0 M in THF, 1.0 mL, 5.0 mmol) was added to an ice-cold solution of nitrile **9b** (400 mg, 1.6 mmol) in THF (5 mL). The mixture was heated under reflux for 1 h when the reaction was placed in an ice-bath and quenched by the slow addition of methanol until bubbling ceased. Solvents removed under reduced pressure and crude product was purified by flash column chromatography giving a colorless oil (163 mg, 40%). HPLC: $t_R = 10.0$ min (96%). ^{1}H NMR (500 MHz, CDCl$_3$) δ 7.22 (t, $J = 8.0$ Hz, 1H), 6.81 – 6.70 (m, 3H), 3.74 (d, $J = 6.4$ Hz, 2H), 2.84 (d, $J = 6.9$ Hz, 2H), 2.71 (h, $J = 7.0$ Hz, 1H), 1.92 – 1.84 (m, 2H), 1.82 – 1.65 (m, 4H), 1.36 – 1.27 (m, 2H), 1.24 (d, $J = 6.8$ Hz, 3H), 1.21 – 1.11 (m, 2H), 1.10 – 1.00 (m, 2H). ^{13}C NMR (126 MHz, CDCl$_3$) δ 159.6, 146.8, 129.5, 119.6, 114.0, 112.0, 73.5, 49.6, 43.8, 37.9, 30.1, 26.6, 25.9, 19.4. HRMS (ES): (m/z) calculated for C$_{16}$H$_{25}$NO [M]$^+$ 247.1936; found 247.1933.

2-(3-(Cyclohexylmethoxy)-4-fluorophenyl)ethan-1-amine (11d).—Nitro compound **10** (414 mg, 1.49 mmol) and lithium aluminum hydride (1M in THF, 5.96 mL, 5.96 mmol) in THF (15 mL) were added to a 200 mL sealed tube to react 24 h at 50 °C with stirring. After cooled to room temperature, the reaction mixture was quenched by 20 mL methanol until bubbling ceased. Solvents removed under reduced pressure and crude product was purified by flash column chromatography giving a yellow oil (297 mg, 80%). HPLC: $t_R = 10.0$ min (94%). ^{1}H NMR (500 MHz, CD$_3$OD) δ 7.03 (dd, $J = 11.2, 8.0$ Hz, 1H), 6.96 (d, $J = 10.0$ Hz, 1H), 6.80–6.76.18 (m, 1H), 3.86 (d, $J = 6.5$ Hz, 2H), 2.91 (t, $J = 14.5$ Hz, 2H), 2.76 (t, $J = 14.5$ Hz, 2H), 1.94-1.74(m, 6H), 1.42-1.10 (m, 5H). ^{13}C NMR (126 MHz, CD$_3$OD) δ 153.8, 151.8, 148.7, 148.6, 137.5, 137.5, 122.0, 122.0, 116.9, 116.7, 116.7, 75.8, 44.3, 39.8, 39.3, 31.0, 27.8, 27.1. ^{19}F NMR (471 MHz, CD$_3$OD) δ −140.08 HRMS (ES): (m/z) calculated for C$_{15}$H$_{22}$FNO [M]$^+$ 251.1686; found 251.1689.

3-(3-(Cyclohexylmethoxy)phenyl)butan-1-amine (*16b*).—Unsaturated nitrile 14 (818 mg, 3.2 mmol) and lithium aluminum hydride (1M in THF, 16 mL, 16 mmol) in THF (40 mL) was added to a 200 mL sealed tube to react for 24 h at 80 °C with stirring. After cooled to room temperature, the reaction mixture was quenched by methanol (80 mL) until bubbling ceased. Solvents removed under reduced pressure and crude product was purified by flash column chromatography giving a yellow oil (225 mg, 27%). HPLC: $t_R = 10.0$ min

(91%). ^{1}H NMR (500 MHz, CD$_3$OD) δ 7.17 (t, J = 16.0 Hz, 1H), 6.77 (d, J = 7.5 Hz, 1H), 6.75 (t, J = 4.5 Hz, 1H), 3.75 (d, J = 6.5 Hz, 2H), 2.77-2.70 (m, 1H), 2.57-2.45(m, 2H), 1.90-1.71(m, 8H), 1.38-1.06 (m, 8H). ^{13}C NMR (126 MHz, CD$_3$OD) δ 161.1, 150.1, 130.5, 120.3, 114.5, 113.0, 74.5, 42.5, 41.1, 39.4, 39.2, 31.2, 27.8, 27.2, 23.2. HRMS (ES): (m/z) calculated for C$_{17}$H$_{27}$NO [M]$^+$ 261.2093; found 261.2090.

(3-(Cyclohexylmethoxy)phenyl)-2-methylpropan-1-amine(16c).—Unsaturated nitrile **15a** (458 mg, 1.8 mmol) and lithium aluminum hydride (1M in THF, 9 mL, 9 mmol) in THF (20 mL) was added to a 200 mL sealed tube to react 24 h at 80 °C with stirring. After cooled to room temperature, the reaction mixture was quenched by methanol (40 mL) until bubbling ceased. Solvents removed under reduced pressure and crude product was purified by flash column chromatography giving a colorless oil (88 mg, 19%). HPLC: t$_R$ = 9.8 min (96%). ^{1}H NMR (500 MHz, CD$_3$OD) δ 7.14 (t, J = 16.0 Hz, 1H), 6.80-6.66 (m, 3H), 3.72 (d, J = 6.5 Hz, 2H), 2.76-2.58 (m, 2H), 2.47-2.30(m, 2H), 1.87-1.69(m, 8H), 1.39-1.03 (m, 6H), 0.88 (d, J = 6.5 Hz, 3H). ^{13}C NMR (126 MHz, CD$_3$OD) δ 160.9, 143.7, 130.3, 122.5, 116.6, 113.0, 74.5, 42.2, 39.3, 39.0, 31.1, 27.8, 27.1, 17.9. HRMS (ES): (m/z) calculated for C$_{17}$H$_{27}$NO [M]$^+$ 261.2093; found 261.2093.

3-(3-(Cyclohexylmethoxy)-4-fluorophenyl)-2-methylpropan-1-amine (16d).— Unsaturated nitrile **15b** (805 mg, 2.95 mmol), palladium on activated carbon (161 mg, 20 wt%), and MeOH (20 mL) were added to a 50 mL round bottom flask. The flask was placed in a high pressure reaction vessel and hydrogenated (200 psi) at room temperature for 36 h with stirring. The reaction mixture was filtered, concentrated under reduced pressure and purified by flash column chromatography giving a pale-yellow oil (320 mg, yield 39%). HPLC: t$_R$ = 10.0 min (97%). ^{1}H NMR (500 MHz, CDCl$_3$) δ 6.92 (dd, J = 11.2, 8 Hz, 2H), 6.72 (d, J = 10 Hz, 1H), 6.62-6.20 (m, 1H), 3.76 (d, J = 5 Hz, 2H), 2.66-2.46 (m, 2H), 2.41-2.28 (m, 2H), 1.87-1.67 (m, 7H), 1.32-0.99 (m, 5H), 0.85 (dd, J = 6.5, 4 Hz, 3H). ^{13}C NMR (126 MHz, CDCl$_3$) δ 151.3 (d, J_{C-F} = 243.2 Hz), 147.1 (d, J_{C-F} = 45.0 Hz), 137.3 (d, J_{C-F} = 3.8 Hz). 121.2 (d, J_{C-F} = 6.3 Hz), 115.8, 115.7(d, J_{C-F} =33.9 Hz), 75.0, 56.3 (d, J_{C-F} = 2.5 Hz), 41.4 (d, J_{C-F} = 6.3 Hz), 37.9, 35.7, 30.0, 26.7,26.0, 18.1. ^{19}F NMR (471 MHz, CDCl$_3$) δ −138.92. HRMS (ES): (m/z) calculated for C$_{17}$H$_{26}$FNO [M]$^+$ 279.1998; found 279.1996.

1-(3-(Cyclohexylmethoxy)phenyl)-3-(methylamino)propan-1-ol (16e).—A solution of 1-(3-(cyclohexylmethoxy)phenyl)propane-1,3-diol (117 mg, 0.34 mmol) and methylamine (2.5 mL, 40% in water) in THF (2.5 mL) was heated at 70 °C for 4 h in pressurized tube. After cooling, the solution was diluted with ether, washed with saturated aqueous sodium bicarbonate and brine, dried with anhydrous potassium carbonate, and concentration to dryness. Purification by flash chromatography gave a colorless oil (80 mg, 85%). HPLC: t$_R$ = 10.8 min (95%). ^{1}H NMR (400 MHz, CDCl3) δ 7.21 (t, J = 8Hz, 1H), 6.92-6.96 (m, 1H), 6.87-6.92 (m, 1H), 6.76 (dd, J = 2.4, 8 Hz, 1H), 4.88 (dd, J = 3.2, 8.4 Hz, 1H), 3.75 (d, J = 6.4 Hz, 2H), 3.46-3.70 (bs, 2H), 2.77-2.91 (m, 2H), 2.42 (s, 3H), 1.82-1.91 (m, 3H), 1.65-1.82 (m, 5H), 1.12-1.35 (m, 3H), 0.98-1.11 (m, 2H); ^{13}C NMR (100 MHz, CDCl3) δ 159.5, 146.9, 129.2, 117.7, 113.1, 111.7, 75.4, 73.5, 50.4, 37.8, 36.9, 36.1, 30.0, 26.6, 25.9. HRMS (ES): (m/z) calculated for C$_{17}$H$_{28}$NO$_2$ [M]$^+$ 277.2042; found 277.2051.

Transformation, Growth, and Purification of CRALBP.

Plasmid (pET19b-CRALBP) was transformed by heat shock into BL-21, which were then grown in LB media at 37 °C until an OD_{600} of 0.5 was obtained. CRALBP expression was then induced additional of IPTG (0.1 mM final concentration) followed by culturing for 14 hours at 22 °C with shaking (200 rpm). Cells were pelleted by centrifugation (10,000g at 4 °C for 15 min), resuspended in buffer, and then subjected to nitrogen cavitation (2×900 psi) with stirring. Lysed cells were centrifuged ($30,000 \times g$ at 4 °C for 30 min) and the supernatant collected. CRALBP was purified by Ni-sepharose chromatography and de-salted on a HiPrep 26/10 column. Fractions were monitored by 280 nm absorbance and collected. Protein concentration was determined by the Bradford assay.

RPE65 Activity Assay *in vitro*.

Synthesized amines in DMF (1 μL) were added to a suspension of microsomal protein (20 mg), 1% bovine serum albumin, 5 mM disodium pyrophosphate, and 16.4 μM apo-retinaldehyde binding protein (CRALBP) in 10 mM BTP (pH = 7.4) buffer to a final concentration between 0 and 10 μM. After 2 min, all-trans retinol (5 mM in DMF, 0.5 μL) was added and the resulting mixture was incubated at 37 °C for 1 h in the dark. Under dim light, the reaction was quenched with methanol (300 μL), extracted with hexanes (300 μL), and all samples were shaken violently by hand for 5 min then stirred at 13000 g for 5 min. The organic layer was collected and 11-cis retinol was quantified by normal phase HPLC using a LUNA prep silica (10 μm, 250×4.6 mm; Phenomenex) column with an isocratic gradient of 10% (v/v) ethyl acetate in hexanes at a flow rate of 1.4 mL/min. Retinoids were detected by monitoring absorbance at 325 and 360 nm and quantified by comparison with a standard curve generated with authentic 11-cis-retinal and retinyl palmitate and area under the curve. Results were normalized by dividing the activity obtained without inhibitor. IC_{50} and relative SD were obtained by fitting the results from each inhibitor using the [Inhibitor] vs normalized response – variable slope function of GraphPad Prism software.

Study animals and approvals.

7 weeks old BALB/cJ albino mice were purchased from the Jackson Laboratory (Jackson Laboratory; Bar Harbor; strain # 000651). Equal numbers of males and females were used for experiments. All mice were housed in the vivarium at the University of California, Irvine, where they were maintained on a normal mouse chow diet and a 12 h/12 h light (<10 lux)/dark cycle. All animal procedures were approved by the Institutional Animal Care and Use Committees (IACUC) of the University of California, Irvine and the VA Long Beach Health Care System and were conducted in accordance with the Association for Research in Vision and Ophthalmology Statement for the Use of Animals in Ophthalmic and Visual Research.

In vivo visual chromophore regeneration assays.

All mice were dark adapted for 24 h prior experiments, and all drug administration procedures were performed under dim red light. One h before the bleaching light exposure, animals were administered test compounds (**3a**, **10b**, **15e**, and **15b-d**) by intraperitoneal (IP) injection at a dose of 10 mg/kg in 50 μL of DMSO vehicle. Vehicle-only and non-treated

animals served as controls. Fifteen min prior to the bleaching light exposure, mice were administered 0.5% tropicamide ophthalmic drops (Patterson Veterinary Supply, Inc) to dilate their pupils. Mice were placed in a 2 L glass beaker contained within a ventilated white bucket and exposed to 10,000 lux white light for 10 minutes. Three animals per group were immediately euthanized and their eyes enucleated, transferred in foil-wrapped tubes, and placed on dry ice. The remaining animals were placed back in their home cages and transferred to a dark room to allow retinoid recovery to occur for either four or 24 hours prior collecting the eyes. Three animals were used for each time point.

The eyes of each animal were homogenized in 10 mM sodium phosphate buffer (pH 8.0) containing 50% methanol (vol/vol) (Sigma–Aldrich; 34860-1L-R) and 100 mM hydroxylamine (Sigma–Aldrich; 159417-100G). After 15 min incubation at room temperature, 2 mL of 3 M sodium chloride were added to the homogenate. The resulting sample was extracted twice with 3 mL ethyl acetate (Fisher Scientific; E195-4). The combined organic phase was dried *in vacuo* and reconstituted in 450 μL hexane. Retinoids extracts (100 μL) were separated on a normal-phase HPLC column (Zorbax Sil; 5 μm; 4.6 mm × 250 mm; Agilent Technologies) with a stepwise gradient of 0.6% v/v ethyl acetate in hexane (Fisher Scientific; H302-4) at a flow rate of 1.4 ml min^{-1} for 17 min and 10 % v/v ethyl acetate in hexane at a flow rate of 1.4 ml min^{-1} for 25 min. Retinoids were detected by monitoring absorbance at 325 nm and 360 nm on Agilent 1200 HPLC system equipped with a diode array detector (DAD). Peaks were identified based on their absorbance spectra and retention times relative to authentic standards. Absolute quantification of retinoids was carried out by peak integration with reference to standard curves generated using authentic standards.

VAP-1 assay.

VAP-1 Oxidation Assay. Mouse aorta homogenates were used as the source of VAP-1 for this study. Aortas were removed from mice (4–6 weeks old) that had been euthanized by CO2 asphyxiation followed by cervical dislocation. The aortas were dissected and the blood was removed by rinsing the tissue with phosphate-buffered saline. Aorta samples were used immediately or stored at −80 °C until needed. Two aortas were minced using a stainless-steel single-edge blade and homogenized in a KONTES Potter-Elvehjem tissue grinder/ homogenizer glass pestle in 1 mL of 10 mM HEPES NaOH, pH 7.6. The homogenate was collected into a 1.5 mL Eppendorf tube. Five μl of a 20 mM ethanolic stock solution of **3a** or **16e** was added to the aorta homogenate to give a final substrate concentration of 100 μM. The sample was mixed and then incubated at 28 °C with 300 rpm shaking in an Eppendorf Thermomixer. 200 μL samples were taken at 0, 1, and 2 h after the initiation of the reaction. At each time point, the reactions were immediately quenched with 100 μL of 100% MeOH, vortexed for 3 s, and stored at −20 °C. After samples from all time points were collected and frozen, the samples were thawed and centrifuged at 15,000 rpm for 10 min; 250 μL of each supernatant was collected, placed into a borosilicate tube, and dried in a Speedvac rotary evaporator. Each dried sample was redissolved in 300 μL of a 1:1 MeOH/H$_2$O solution, centrifuged to remove particulates, and then transferred to an HPLC vial. 50 μL of the sample was used for analysis on an Agilent 1260 Infinity series HPLC equipped with a Proshell EC-18 column and a diode array detector. The sample was separated using a mobile

phase consisting of 0.1% (v/v) formic acid in H_2O and acetonitrile at the following ratios and time intervals: 95:5 for 2 min, a gradient from 95:5 to 15:85 over 8 min, a gradient from 15:85 to 2:98 over 0.5 min, continued 2:98 for 4 min, and then a gradient from 2:98 to 95:5 over 0.5 min. The reaction substrate and product were assessed by monitoring absorbance at 275 nm. **3a** and **16e** were eluted at ~8.5 min, while the assay product (ACU-5201) was eluted at ~13.25 min. A dilution series of known concentrations of authentic ACU-5201 in 1:1 MeOH/H_2O was run to generate a standard curve and facilitate the conversion of product AUCs to absolute concentration.

Liver microsomes assay.

Mouse liver homogenates were used as the source for this study following a published protocol.[44] Briefly, Livers were removed from mice (4–6 weeks old) that had been euthanized by CO_2 asphyxiation followed by cervical dislocation. The livers were dissected and the blood was removed by rinsing the tissue with phosphate-buffered saline. Liver samples were used immediately or stored at −80 °C until needed. Two livers were minced using a stainless-steel single-edge blade and homogenized in a KONTES Potter-Elvehjem tissue grinder/homogenizer glass pestle in 1 mL of 10 mM PBS/10mM KCl, pH 7.4. The microsomes were subsequently stored in 0.1M PBS/20% glycerol, pH 7.4. Assay: to a tube containing 415.6 μL of 0.1M PBS buffer at pH 7.4 pre-warmed at 37°C, 50 μL of NADPH 10 mM, and the appropriate volumes of a 10 mM ethanolic stock solution of **3a**, **16e** or atomoxetine to get a final concentration of 15-200 μM in 500 μL , were added 30 μL of liver homogenate at the concentration of 8.5 mg of protein/mL to achieve a final protein concentration of 0.5 mg/mL. The sample was mixed and then incubated at 37 °C with 300 rpm shaking in an Eppendorf Thermomixer. 100 μL samples were taken at 0, 5, 15, 30 and 60 minutes after the initiation of the reaction. At each time point, the reactions were immediately quenched with 100 μL of 100% MeOH, vortexed for 3 s, and stored at −20 °C. After samples from all time points were collected and frozen, the samples were thawed and centrifuged at 15,000 rpm for 10 min; each supernatant was collected, placed into a borosilicate tube, and dried in a Speedvac rotary evaporator. Each dried sample was redissolved in 200 μL of a 1:1 MeOH/H_2O solution, centrifuged to remove particulates, and then transferred to an HPLC vial. 50 μL of the sample was used for analysis on an Agilent 1260 Infinity series HPLC equipped with a Gemini® 5μM C-18 110 Å column (250 × 4.6 mm) and a diode array detector. The sample was separated using a mobile phase consisting of 1% (v/v) triethylamine in H_2O and acetonitrile at the following ratios and time intervals: 80:20 for 2 min, a gradient from 80:20 to 2:98 over 15 min, continued 2:98 for 2 min, and then a gradient from 2:98 to 80:20 over 8 min continued 80:20 for 2 min. The reaction substrate and product were assessed by monitoring absorbance at 275 nm. **3a**, **16e** and Atomoxetine were eluted at ~14 min, 12 and 15 minutes. A dilution series of known concentrations of authentic **3a**, **16e** and Atomoxetine in 1:1 MeOH/H_2O was run to generate a standard curve and facilitate the conversion of product AUCs to absolute mass.

Quantification of 16e and 3a levels in the serum and eyes of mice after intraperitoneal injection.

8-week-old C57BL/6J mice were treated with a 380 nmol of **16e** in dimethyl sulfoxide (50 μL) by intraperitoneal injection and sacrificed at 1 h, 4 h, or 24 h later. Vehicle

alone (dimethylsulfoxide) and 380 nmol of **3a** were injected as control and the animals were sacrificed at 1 h. Blood and eyeball samples were collected. After clotting at room temperature for 30 min, the blood samples were centrifuged for 10 min at 17,000g in a temperature-controlled benchtop centrifuge (Eppendorf AG). Each serum sample (100 μL) was carefully removed to avoid disturbing loose clots, precipitated with 100 μL of pre-cooled methanol, and centrifuged at 1,500g for 15 min at 4 °C. The supernatant was carefully transferred to a SpinX centrifuge tube filter with a 0.45 μm cellulose acetate membrane (Costar, Salt Lake City, UT) and centrifuged at 7000g for 2 min. The filtered samples were dried under vacuum, reconstituted in 100 μL of 50% methanol/water, and centrifuged at 23,000g for 15 min at 4 °C. The resulting supernatants were ready for LC/MS analyses. The two eyeballs from each mouse were homogenized in pre-cooled methanol (2 × 800 μL). The resulting mixture was centrifuged at 23,000g for 15 min at 4 °C. The supernatant was dried under vacuum, reconstituted in 100 μL of 50% methanol/water, and centrifuged at 23,000g for 15 min at 4 °C. Five microliters of the supernatant extracted from the serum or eye samples was injected into an Vanquish HPLC system coupled with a Q-Exactive mass spectrometer (ThermoFisher Scientific, Waltham, MA) with an ESI unit. The separation was performed on a Proshell EC-18 column (2.7 μm, 3.0 × 150 mm, Agilent, Santa Clara, CA) using a mobile phase consisting of 0.1% aqueous formic acid (A) and acetonitrile (B) at a flow rate of 600 μL·min^{-1}, and the mobile-phase gradients and time course were as follows: 0–2 min, 95% A/5% B; 2–10 min, 95–15% A/5–85% B. The signals of emixustat were detected in the parallel reaction monitoring mode with collision energy 25%. The peaks represent the fragment at m/z 217.2 were quantified. The signals of **16e** and **3a** were detected in the selected ion monitoring mode. The peaks at 7.61 min with m/z 264.2 were quantified. The standards were prepared by using the matrix obtained from the plasma and the eye of untreated animals.

Statistics.

Data are presented as means ± SD, with the number of biological or technical replicates indicated in the figure legends. Curve fitting was performed by non-linear least-squares methods as implemented in GraphPad Prism.

RPE65 crystallization and structure determination.

Crystals of RPE65 in the complex with **16e** were obtained using previously described procedures. Briefly, isolated bovine RPE membranes were incubated with 2.5 mM of **16e** [delivered in dimethylformamide (DMF)] for 15 min prior to solubilization with 24 mM hexaethylene glycol mono-octyl ether (C8E6). After anion-exchange chromatography, purified RPE65 was concentrated to 10–15 mg/mL and **16e** was added again to a concentration of 2.5 mM prior to crystallization. Crystals were grown by the hanging-drop vapor-diffusion method by mixing 2 μL of a 10 mg/mL RPE65 sample with 2 μL of crystallization solution consisting of 30% v/v PEG 400, 100 mM CAPS, pH 10.5, 500 mM $(NH_4)_2SO_4$, and 10% v/v glycerol. After incubation for 1-2 weeks at 8 °C, crystals of approximately 100 × 100 × 300 μm in size were observed. Mature crystals were harvested directly into liquid nitrogen for X-ray data collection. X-ray diffraction data were collected at the APS NE-CAT 24-ID-E beamlines. Data were processed using XDS,[45, 46] and the initial model was obtained by direct refinement using published RPE65 coordinates

in which ligands had been removed (PDB accession code: 4RYX). The structure was refined by alternating reciprocal space refinement in REFMAC and manual building and adjustments in Coot.[47] Ligand coordinates and geometry dictionary files were generated using the Grade server (http://grade.globalphasing.org/cgi-bin/grade/server). The models were validated using MolProbity[48] and the wwPDB validation server.[49]

Supplementary Material

Refer to Web version on PubMed Central for supplementary material.

REFERENCES

(1). McBee JK; Palczewski K; Baehr W; Pepperberg DR Confronting complexity: the interlink of phototransduction and retinoid metabolism in the vertebrate retina. Prog. Retin. Eye Res. 2001, 20 (4), 469–529. [PubMed: 11390257]

(2). Kiser PD; Golczak M; Palczewski K Chemistry of the retinoid (visual) cycle. Chem. Rev 2014, 114 (1), 194–232. [PubMed: 23905688]

(3). Kefalov VJ Rod and cone visual pigments and phototransduction through pharmacological, genetic, and physiological approaches. J. Biol. Chem 2012, 287 (3), 1635–1641. [PubMed: 22074928]

(4). Kiser PD; Palczewski K Pathways and disease-causing alterations in visual chromophore production for vertebrate vision. J. Biol. Chem 2021, 296, 100072. [PubMed: 33187985]

(5). Kiser PD Retinal pigment epithelium 65 kDa protein (RPE65): An update. Prog. Retin. Eye Res 2022, 88, 101013. [PubMed: 34607013]

(6). Chen Y; Okano K; Maeda T; Chauhan V; Golczak M; Maeda A; Palczewski K Mechanism of all-trans-retinal toxicity with implications for stargardt disease and age-related macular degeneration. J. Biol. Chem 2012, 287 (7), 5059–5069. [PubMed: 22184108]

(7). Liu H; Tang J; Du Y; Lee CA; Golczak M; Muthusamy A; Antonetti DA; Veenstra AA; Amengual J; von Lintig J; et al. Retinylamine Benefits Early Diabetic Retinopathy in Mice. J. Biol. Chem 2015, 290 (35), 21568–21579. [PubMed: 26139608]

(8). Lessieur EM; Du Y; Saadane A; Liu H; Kiser J; Kern TS Partial deletion of Lrat inhibits prodromal characteristics of diabetic retinopathy. Invest. Ophthalmol. Vis. Sci 2022, 63 (7), 3590 – A0045–3590 – A0045.

(9). Grimm C; Wenzel A; Hafezi F; Yu S; Redmond TM; Reme CE Protection of Rpe65-deficient mice identifies rhodopsin as a mediator of light-induced retinal degeneration. Nat. Genet 2000, 25 (1), 63–66. [PubMed: 10802658]

(10). Saari JC; Nawrot M; Kennedy BN; Garwin GG; Hurley JB; Huang J; Possin DE; Crabb JW Visual cycle impairment in cellular retinaldehyde binding protein (CRALBP) knockout mice results in delayed dark adaptation. Neuron 2001, 29 (3), 739–748. [PubMed: 11301032]

(11). Golczak M; Kuksa V; Maeda T; Moise AR; Palczewski K Positively charged retinoids are potent and selective inhibitors of the trans-cis isomerization in the retinoid (visual) cycle. Proc. Natl. Acad. Sci. U. S. A 2005, 102 (23), 8162–8167. [PubMed: 15917330]

(12). Zhang J; Dong Z; Mundla SR; Hu XE; Seibel W; Papoian R; Palczewski K; Golczak M Expansion of first-in-class drug candidates that sequester toxic all-trans-retinal and prevent light-induced retinal degeneration. Mol. Pharmacol 2015, 87 (3), 477–491. [PubMed: 25538117]

(13). Zhang J; Kiser PD; Badiee M; Palczewska G; Dong Z; Golczak M; Tochtrop GP; Palczewski K Molecular pharmacodynamics of emixustat in protection against retinal degeneration. J. Clin. Invest 2015, 125 (7), 2781–2794. [PubMed: 26075817]

(14). Kiser PD; Zhang J; Badiee M; Kinoshita J; Peachey NS; Tochtrop GP; Palczewski K Rational Tuning of Visual Cycle Modulator Pharmacodynamics. J Pharmacol Exp Ther 2017, 362 (1), 131–145. [PubMed: 28476927]

(15). Blum E; Zhang J; Zaluski J; Einstein DE; Korshin EE; Kubas A; Gruzman A; Tochtrop GP; Kiser PD; Palczewski K Rational Alteration of Pharmacokinetics of Chiral Fluorinated and Deuterated Derivatives of Emixustat for Retinal Therapy. J. Med. Chem 2021, 64 (12), 8287–8302. [PubMed: 34081480]

(16). Maeda A; Golczak M; Chen Y; Okano K; Kohno H; Shiose S; Ishikawa K; Harte W; Palczewska G; Maeda T; et al. Primary amines protect against retinal degeneration in mouse models of retinopathies. Nat. Chem. Biol 2011, 8 (2), 170–178. [PubMed: 22198730]

(17). Sparrow JR; Gregory-Roberts E; Yamamoto K; Blonska A; Ghosh SK; Ueda K; Zhou J The bisretinoids of retinal pigment epithelium. Prog. Retin. Eye Res 2012, 31 (2), 121–135. [PubMed: 22209824]

(18). Walia S; Fishman GA Natural history of phenotypic changes in Stargardt macular dystrophy. Ophthalmic Genet. 2009, 30 (2), 63–68. [PubMed: 19373676]

(19). Haji Abdollahi S; Hirose T Stargardt-Fundus flavimaculatus: recent advancements and treatment. Semin. Ophthalmol 2013, 28 (5–6), 372–376. [PubMed: 24138045]

(20). Maeda A; Maeda T; Golczak M; Chou S; Desai A; Hoppel CL; Matsuyama S; Palczewski K Involvement of all-trans-retinal in acute light-induced retinopathy of mice. J. Biol. Chem 2009, 284 (22), 15173–15183. [PubMed: 19304658]

(21). Pang JJ; Chang B; Hawes NL; Hurd RE; Davisson MT; Li J; Noorwez SM; Malhotra R; McDowell JH; Kaushal S; et al. Retinal degeneration 12 (rd12): a new, spontaneously arising mouse model for human Leber congenital amaurosis (LCA). Mol. Vis 2005, 11, 152–162. [PubMed: 15765048]

(22). Redmond TM; Yu S; Lee E; Bok D; Hamasaki D; Chen N; Goletz P; Ma JX; Crouch RK; Pfeifer K Rpe65 is necessary for production of 11-cis-vitamin A in the retinal visual cycle. Nat. Genet 1998, 20 (4), 344–351. [PubMed: 9843205]

(23). Kiser PD; Palczewski K Retinoids and Retinal Diseases. Annu. Rev. Vis. Sci 2016, 2, 197–234. [PubMed: 27917399]

(24). McBee JK; Kuksa V; Alvarez R; de Lera AR; Prezhdo O; Haeseleer F; Sokal I; Palczewski K Isomerization of all-trans-retinol to cis-retinols in bovine retinal pigment epithelial cells: dependence on the specificity of retinoid-binding proteins. Biochemistry 2000, 39 (37), 11370–11380. [PubMed: 10985782]

(25). Law WC; Rando RR The molecular basis of retinoic acid induced night blindness. Biochem. Biophys. Res. Commun 1989, 161 (2), 825–829. [PubMed: 2660792]

(26). Scott IL; Kuksa VA; Orme MW; Little T; Gall A; Hong F Alkoxy compounds for disease treatment. US 11,446,261 B2, 2014.

(27). Kubota R; Al-Fayoumi S; Mallikaarjun S; Patil S; Bavik C; Chandler JW Phase 1, dose-ranging study of emixustat hydrochloride (ACU-4429), a novel visual cycle modulator, in healthy volunteers. Retina 2014, 34 (3), 603–609. [PubMed: 24056528]

(28). Kubota R; Birch DG; Gregory JK; Koester JM Randomised study evaluating the pharmacodynamics of emixustat hydrochloride in subjects with macular atrophy secondary to Stargardt disease. Br. J. Ophthalmol 2022, 106 (3), 403–408. [PubMed: 33214244]

(29). Kubota R; Boman NL; David R; Mallikaarjun S; Patil S; Birch D Safety and effect on rod function of ACU-4429, a novel small-molecule visual cycle modulator. Retina 2012, 32 (1), 183–188. [PubMed: 21519291]

(30). Kubota R; Calkins DJ; Henry SH; Linsenmeier RA Emixustat Reduces Metabolic Demand of Dark Activity in the Retina. Invest. Ophthalmol. Vis. Sci 2019, 60 (14), 4924–4930. [PubMed: 31770432]

(31). Kubota R; Gregory J; Henry S; Mata NL Pharmacotherapy for metabolic and cellular stress in degenerative retinal diseases. Drug Discov. Today 2020, 25 (2), 292–304. [PubMed: 31809750]

(32). Kubota R; Jhaveri C; Koester JM; Gregory JK Effects of emixustat hydrochloride in patients with proliferative diabetic retinopathy: a randomized, placebo-controlled phase 2 study. Graefes Arch. Clin. Exp. Ophthalmol 2021, 259 (2), 369–378. [PubMed: 32852613]

(33). Kiser PD; Zhang J; Badiee M; Li Q; Shi W; Sui X; Golczak M; Tochtrop GP; Palczewski K Catalytic mechanism of a retinoid isomerase essential for vertebrate vision. Nat. Chem. Biol 2015, 11 (6), 409–415. [PubMed: 25894083]

(34). Dugel PU; Novack RL; Csaky KG; Richmond PP; Birch DG; Kubota R Phase ii, randomized, placebo-controlled, 90-day study of emixustat hydrochloride in geographic atrophy associated with dry age-related macular degeneration. Retina 2015, 35 (6), 1173–1183. [PubMed: 25932553]

(35). Rosenfeld PJ; Dugel PU; Holz FG; Heier JS; Pearlman JA; Novack RL; Csaky KG; Koester JM; Gregory JK; Kubota R Emixustat Hydrochloride for Geographic Atrophy Secondary to Age-Related Macular Degeneration: A Randomized Clinical Trial. Ophthalmology 2018, 125 (10), 1556–1567. [PubMed: 29716784]

(36). Reid MJ; Eyre R; Podoll T Oxidative Deamination of Emixustat by Human Vascular Adhesion Protein-1/Semicarbazide-Sensitive Amine Oxidase. Drug Metab. Dispos 2019, 47 (5), 504–515. [PubMed: 30787099]

(37). Smith DJ; Salmi M; Bono P; Hellman J; Leu T; Jalkanen S Cloning of vascular adhesion protein 1 reveals a novel multifunctional adhesion molecule. J. Exp. Med 1998, 188 (1), 17–27. [PubMed: 9653080]

(38). Fitzsimmons ME; Sun G; Kuksa V; Reid MJ Disposition, profiling and identification of emixustat and its metabolites in humans. Xenobiotica 2018, 48 (6), 592–604. [PubMed: 28678597]

(39). Golczak M; Imanishi Y; Kuksa V; Maeda T; Kubota R; Palczewski K Lecithin:retinol acyltransferase is responsible for amidation of retinylamine, a potent inhibitor of the retinoid cycle. J. Biol. Chem 2005, 280 (51), 42263–42273. [PubMed: 16216874]

(40). Gong B; Boor PJ The role of amine oxidases in xenobiotic metabolism. Expert Opin. Drug Metab. Toxicol 2006, 2 (4), 559–571. [PubMed: 16859404]

(41). Benedetti MS Biotransformation of xenobiotics by amine oxidases. Fundam. Clin. Pharmacol 2001, 15 (2), 75–84. [PubMed: 11468017]

(42). Claud P; Padovani P; Guichard JP; Artur Y; Laine R Involvement of semicarbazide-sensitive amine oxidase in tresperimus metabolism in human and in rat. Drug Metab. Dispos 2001, 29 (5), 735–741. [PubMed: 11302941]

(43). Wang Y; Ma X; Muthuraman P; Raja A; Jayaraman A; Petrukhin K; Cioffi CL; Ma JX; Moiseyev G The novel visual cycle inhibitor (+/−)-RPE65-61 protects retinal photoreceptors from light-induced degeneration. PLoS One 2022, 17 (10), e0269437. [PubMed: 36227868]

(44). Knights KM; Stresser DM; Miners JO; Crespi CL In Vitro Drug Metabolism Using Liver Microsomes. Curr. Protoc. Pharmacol 2016, 74, 7 8 1–7 8 24.

(45). Kabsch W Integration, scaling, space-group assignment and post-refinement. Acta Crystallogr. D Biol. Crystallogr 2010, 66 (Pt 2), 133–144. [PubMed: 20124693]

(46). Kabsch W Xds. Acta Crystallogr. D Biol. Crystallogr 2010, 66 (Pt 2), 125–132. [PubMed: 20124692]

(47). Emsley P; Lohkamp B; Scott WG; Cowtan K Features and development of Coot. Acta Crystallogr. D Biol. Crystallogr 2010, 66 (Pt 4), 486–501. [PubMed: 20383002]

(48). Williams CJ; Headd JJ; Moriarty NW; Prisant MG; Videau LL; Deis LN; Verma V; Keedy DA; Hintze BJ; Chen VB; et al. MolProbity: More and better reference data for improved all-atom structure validation. Protein Sci. 2018, 27 (1), 293–315. [PubMed: 29067766]

(49). Read RJ; Adams PD; Arendall WB 3rd; Brunger AT; Emsley P; Joosten RP; Kleywegt GJ; Krissinel EB; Lutteke T; Otwinowski Z; et al. A new generation of crystallographic validation tools for the protein data bank. Structure 2011, 19 (10), 1395–1412. [PubMed: 22000512]
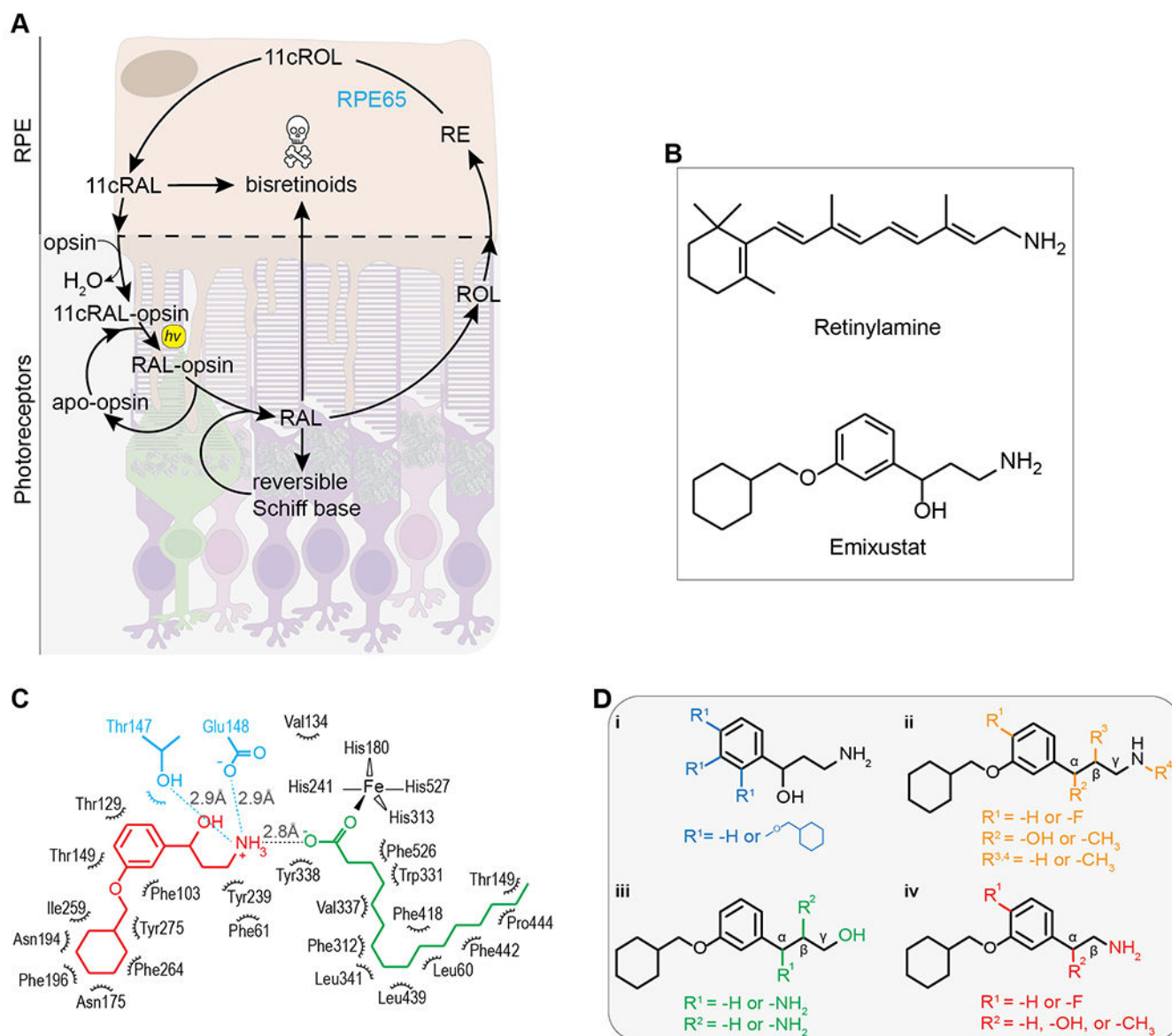
Figure 1:

Inhibition of visual cycle using emixustat-like inhibitors. **(A)** Emixustat inhibits a crucial step of the visual cycle by blocking the isomerization of all-*trans*-RE to 11-*cis*-ROL catalyzed by RPE65. Abbreviations: *hv*, photon; 11cROL, 11-*cis*-retinol; 11cRAL, 11-*cis*-retinal; RAL, all-*trans*-retinal; ROL, all-*trans*-retinol; RE, retinyl-esters; RPE65, retinal pigment epithelium protein 65 kDa. **(B)** Chemical structure of targeted-RPE65 inhibitors. **(C)**Two-dimensional interaction diagram for emixustat (red) and palmitate (green) ligands in RPE65's active site. Polar interactions are represented with dashed lines. Residues involved in non-dipolar interactions are shown as spiked arcs. **(D)** Modifications of emixustat's scaffold described here: (**i**) γ-amino-α-propanol geometric derivatives (parent molecule is in the meta configuration); (**ii**) methylated derivatives; (**iii**) α/β-amino-γ-propanol derivatives; (**iv**) truncated analogs.
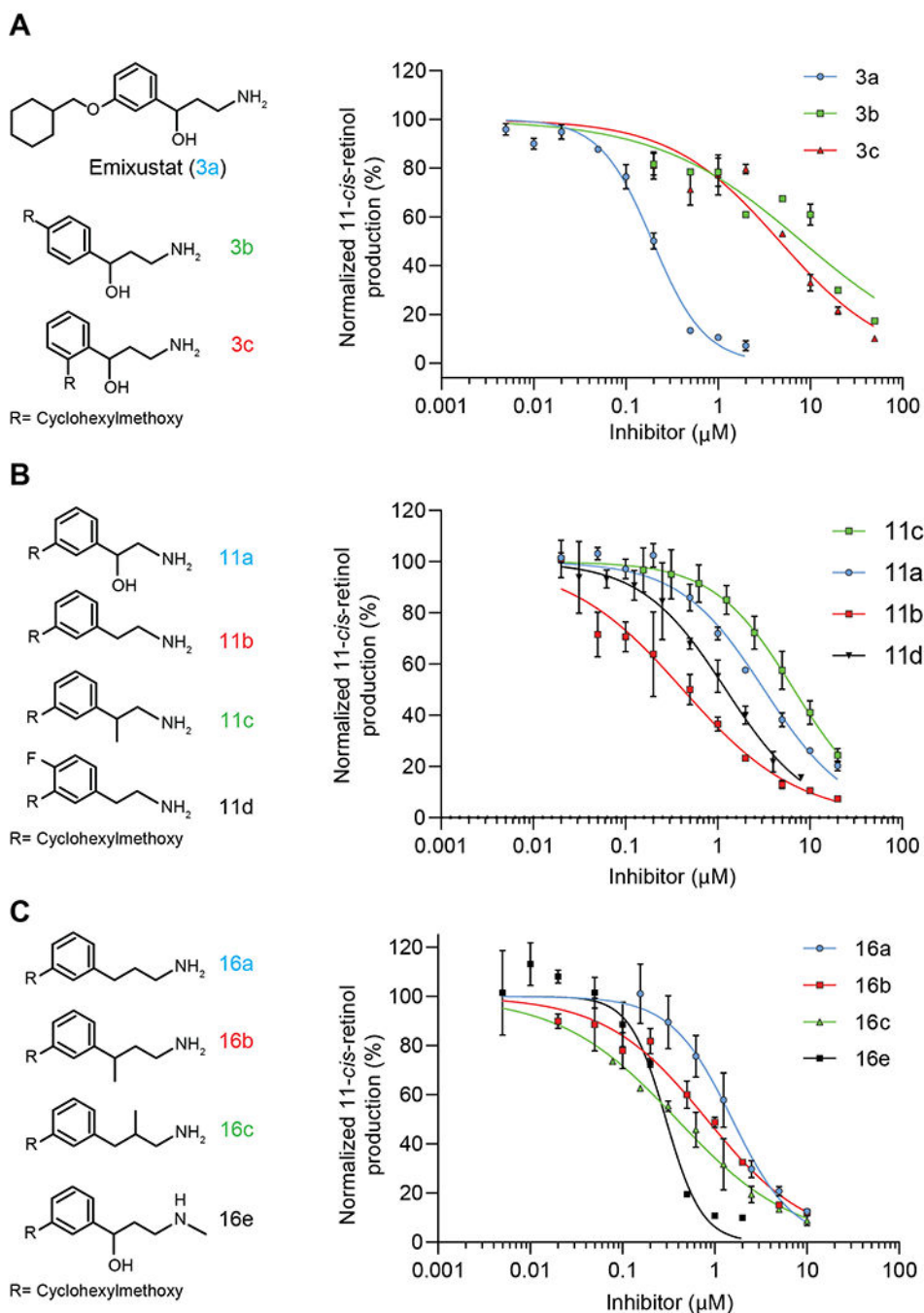
Figure 2:

In vitro inhibition of RPE65 isomerase by synthesized compounds. Chemical structures and corresponding dose response curves of **A**) γ-amino-α-aryl alcohols **3a** – **c**, **B**) ethylamines **11a** – **d**, and **C**) propylamines **16a** – **c** and **16e**. All data points are plotted as mean ± SD representing 3 replicates per point.
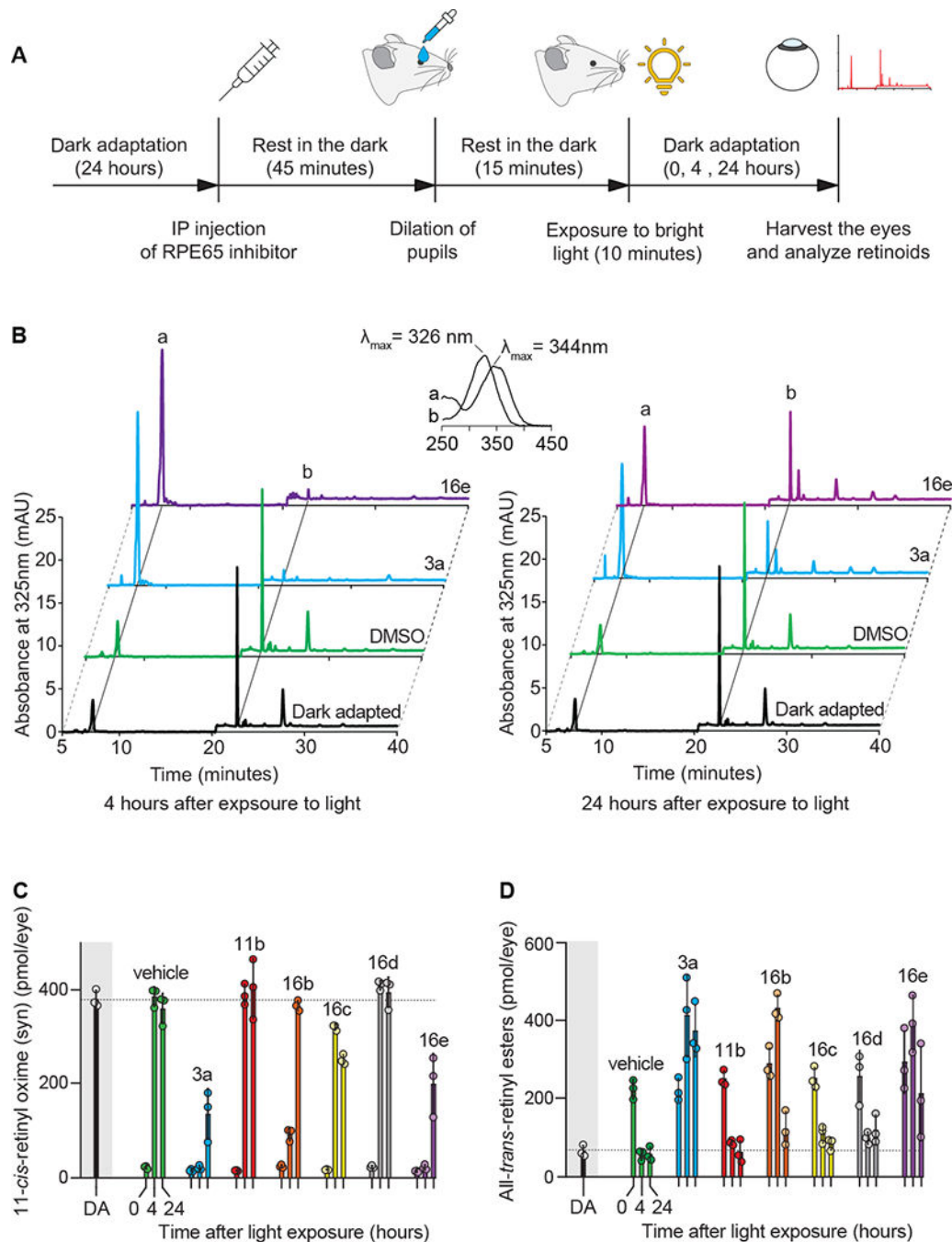
Figure 3:

Inhibition of RPE65 *in vivo*. **(A)** Illustration showing the timeline of the experiment. IP, intraperitoneal injection. **(B)** Representative HPLC chromatograms obtained from retinoid extracts of dark-adapted mice (black trace), and mice treated with vehicle (DMSO, green line), **3a** (blue trace) and **16e** (purple trace) that were dark adapted for four (left panel) and 24 hours (right panel) after exposure to light. The two solid lines indicate the peaks corresponding to the RE (a) and the 11cRAL oxime (syn) (b). Insets show the spectral identity of 11cRAL oxime (syn) (a) and the RE (b) respectively. **(C-D)** Kinetics of 11cRAL

synthesis and RE clearance after IP injection of vehicle or test compounds for RPE65 inhibition. The dashed line indicates mean baseline levels of 11cRAL and RE from dark-adapted mice. Mean values ± SD, n = 3 and individual data points are shown in the graph.
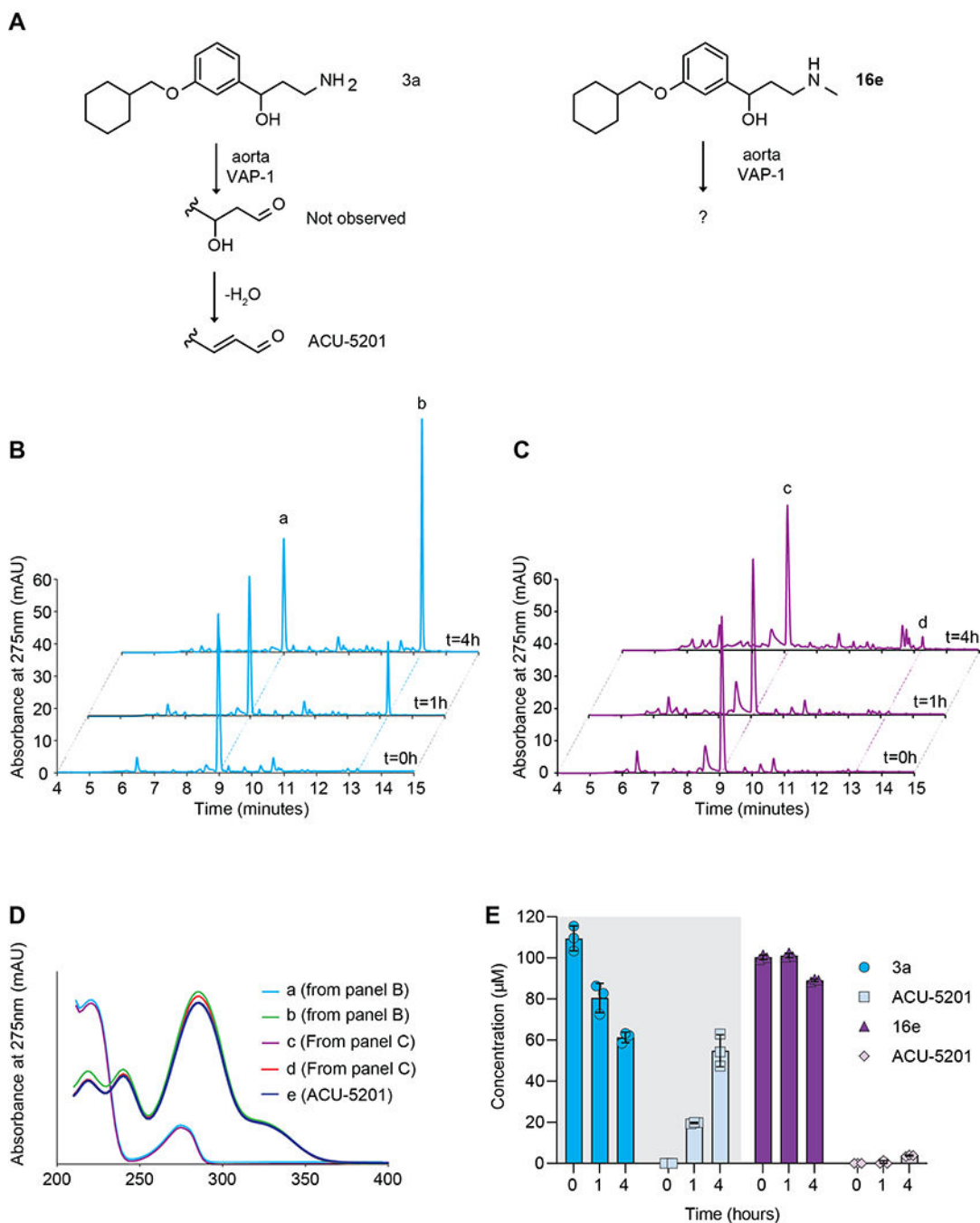
Figure 4:

Test of VAP-1-dependent oxidative metabolism of compound 16e. **(A)** Scheme showing the oxidation of **3a** (left) and **16e** (right) by VAP-1 present in the aorta homogenates used for the assay. **(B-C)** Representative HPLC chromatograms obtained from homogenates of mice aortas showing the time course of oxidative metabolism by VAP-1 on **3a** (blue traces) and **16e** (purple traces). **(D)** Comparison between the UV/vis absorbance spectra of the peaks labeled in panels B-C and the UV/vis absorbance spectra of the synthetic standard ACU-5201. **(E)** Kinetics of product formation for **3a** (blue columns) and **16e** (purple

columns). Mean values ± SD, n = 3 replicates and individual data points are shown in the graph.
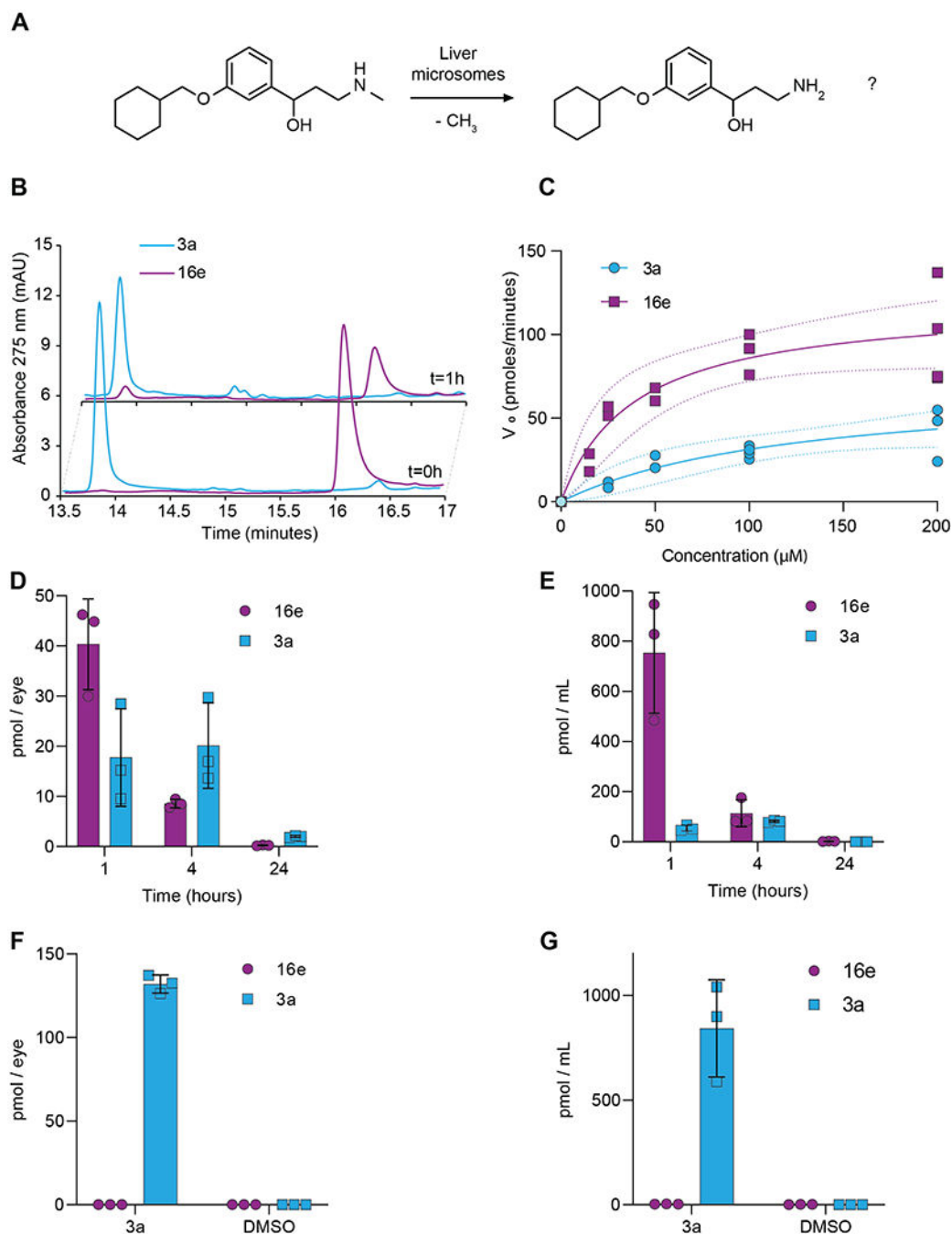
Figure 5:

Evaluation of 16e hepatic metabolism. **(A)** Scheme illustrating the possible synthesis of **3a** from **16e** in liver microsomes. **(B)** Representative HPLC chromatograms obtained from liver microsomes showing the time course of **3a** (blue traces) and **16e** (purple traces) metabolism. **3a** and **16e** were used at a concentration of 200 μM. **(C)** Plot showing the relationship between V_0 and concentration of **3a** (blue trace) and **16e** (purple trace). Single data are plotted and fitted with Michaelis-Menten equation using GraphPad software. 90% confidence intervals are shown as dotter liens. Progress of **16e** elimination in the mouse eye

(**D**) and serum (**E**). Mean values ± SD, n = 3 replicates and individual data points are shown in the graph. Quantification of **16e** and **3a** in the mouse eye (**F**) and serum (**G**) one hour after receiving an intraperitoneal injection of **3a** or vehicle (DMSO), Mean values ± SD, n = 3 replicates and individual data points are shown in the graph.
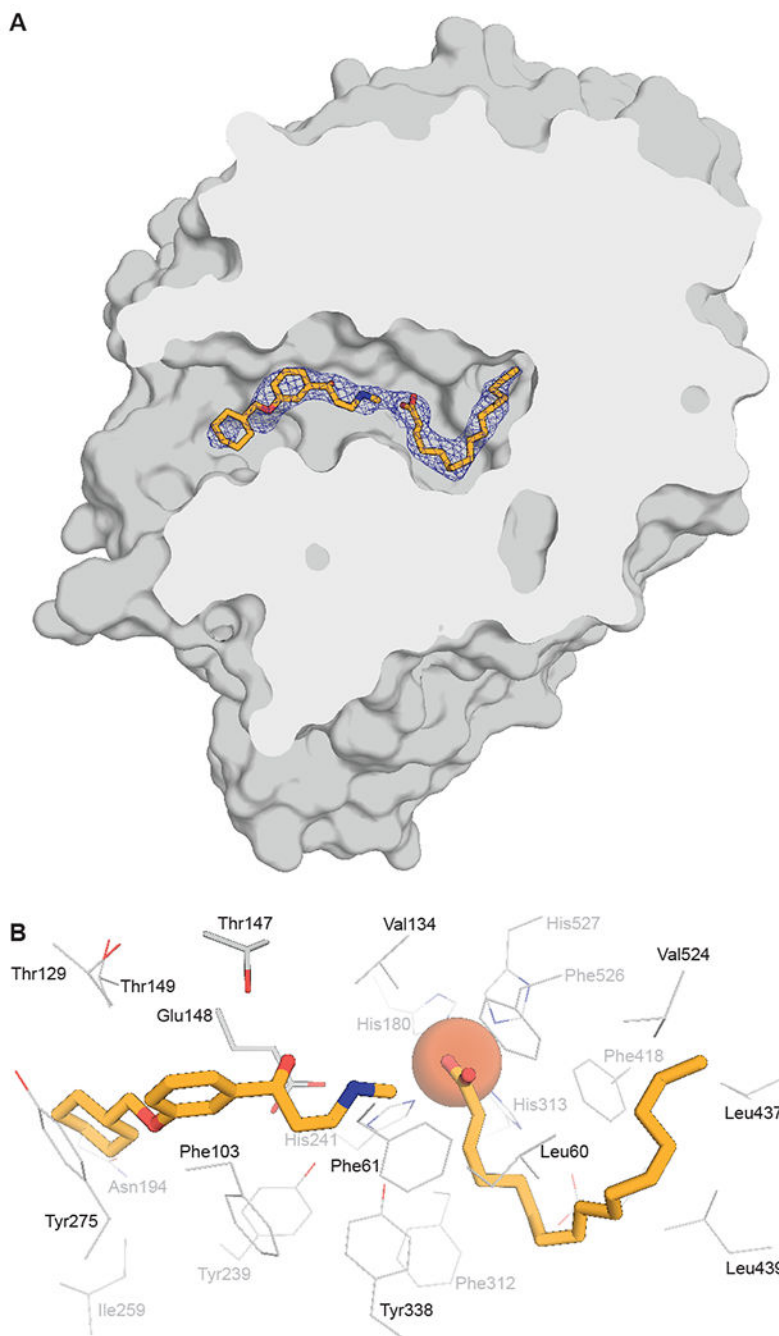
Figure 6:
Crystal structure of RPE65 in complex with **16e**. (**A**) Cut-through view of the RPE65 active site showing the binding location of **16e** as well as a coordinated palmitate ligand. The corresponding $2F_0 - F_c$ electron density map, contoured at 1 RMSD, is shown as blue mesh within 2 Å of the bound ligands. (**B**) Illustration of RPE65 residues within 4.5 Å from the bound ligands. Thr147 and Glu148, which are suggested to be important for inhibitor binding, are shown as grey sticks. The PDB accession code for the structure 8DOC.
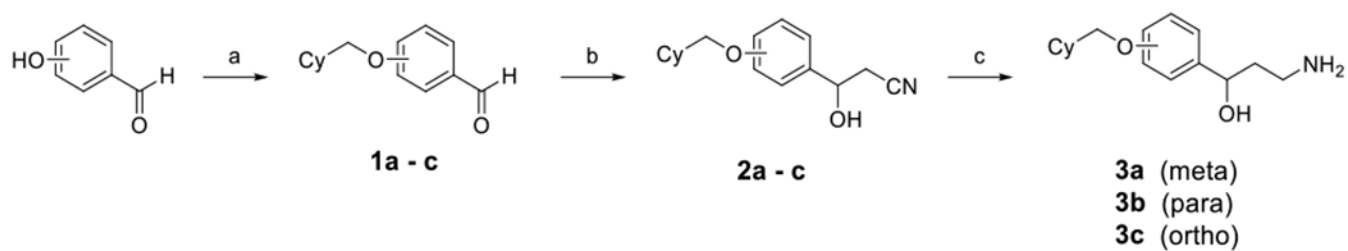
Scheme 1: Synthesis of Emixustat γ-Amino-α-Aryl Propanols.[a]
[a]Reagents and Conditions: (a) Cyclohexylmethyl bromide, K_2CO_3, DMF, 90 °C, overnight;
(b) LDA, MeCN, THF, −78 °C, 3 h; (c) LAH, THF, 0 °C, 1 h.
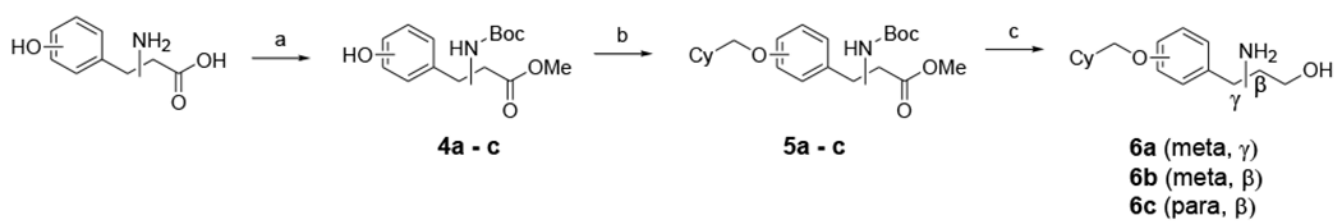
Scheme 2: Synthesis of γ and β-Amino-γ-Aryl Propanols.[a]

[a]Reagents and Conditions: (a) i) MeOH, conc. H_2SO_4, NaCl, RT; ii) Boc_2O, MeCN, NEt_3, RT, 2 h; (b) K_2CO_3, Cyclohexylmethyl bromide, DMF, 90 °C, overnight; c) i) LAH, THF, 0 °C, 1 h; ii) TFA, DCM, RT, 1 h.
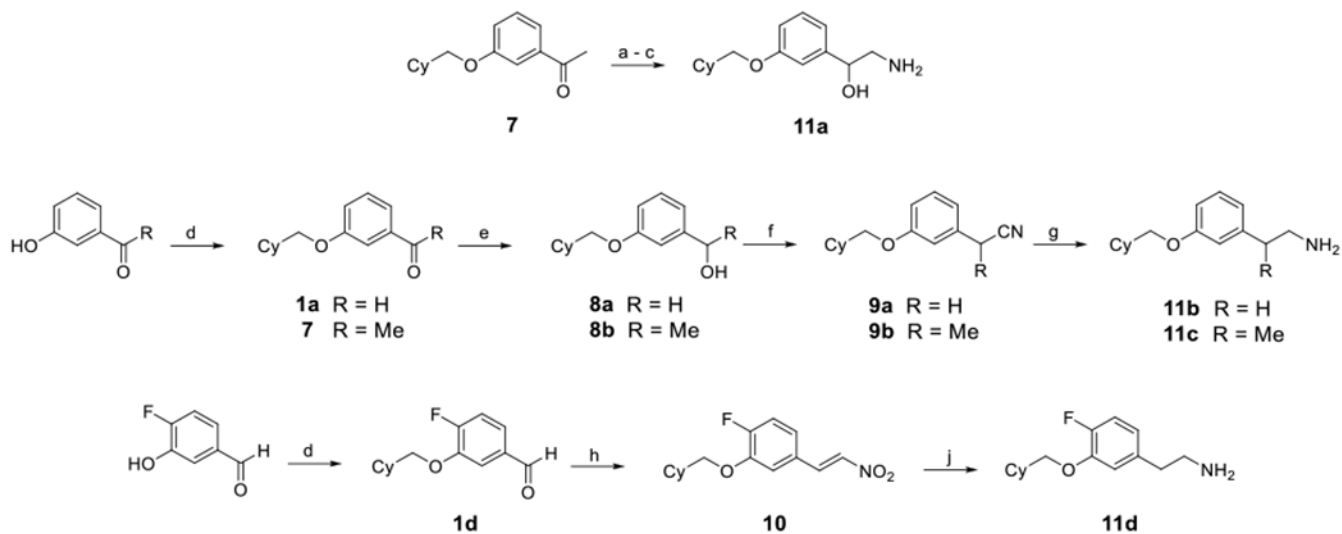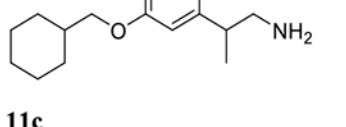
Scheme 3: Synthesis of (3-cyclohexylmethoxy)phenylethan-amines.[a]

[a]Reagents and Conditions: (a) pyridinium tribromide, DCM, RT, 2 h; (b) NaN$_3$, DMF, 50 °C, 0.5 h; (c) LAH, THF, 0 °C, 1 h; (d) Cyclohexylmethyl bromide, K$_2$CO$_3$, DMF, 90 °C, overnight; (e) NaBH$_4$, MeOH, RT, 2 h; (f) i) PBr$_3$, ether, hexanes, RT, overnight; ii) KCN, DMF, overnight; (g) i) BH$_3$, THF, reflux, 1 h; ii) MeOH, 0 °C; (h) MeNO$_2$, NH$_4$OAc, 120 °C, 1 h; (j) LAH, THF, 50 °C, 24 h.
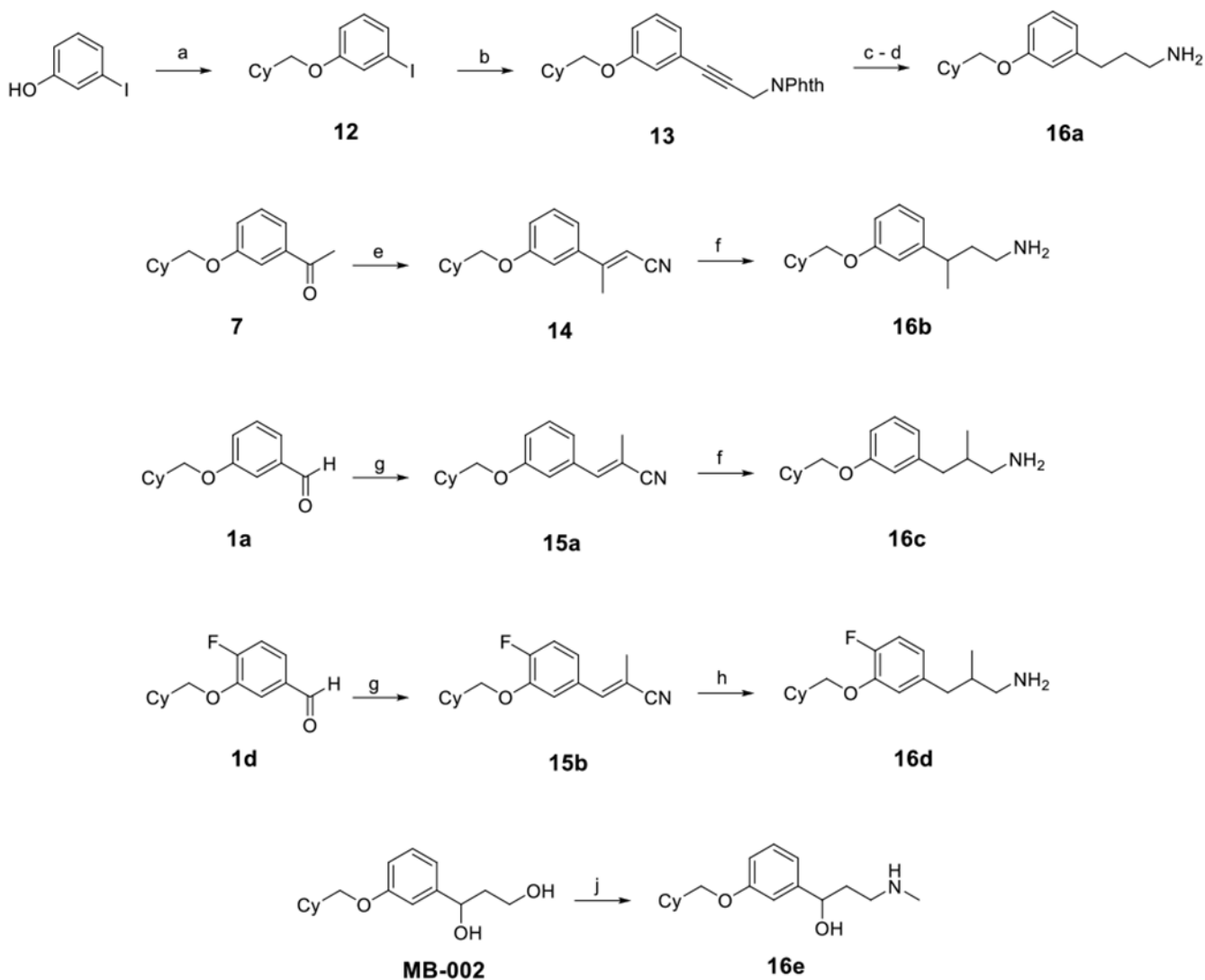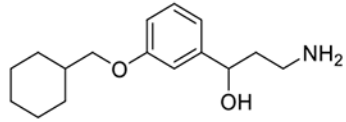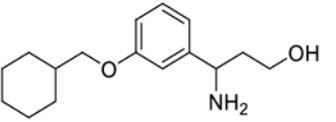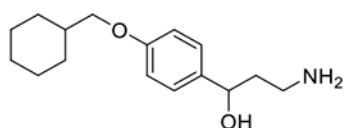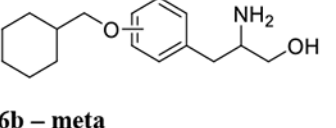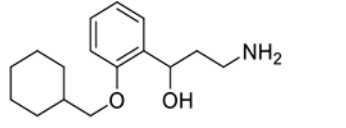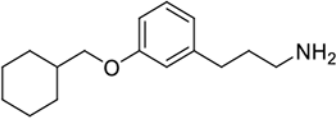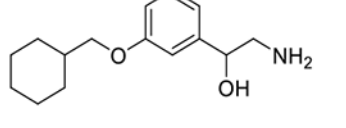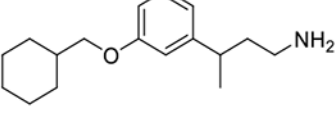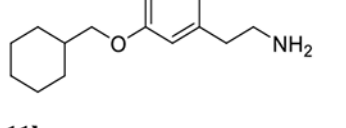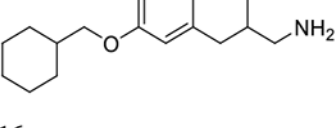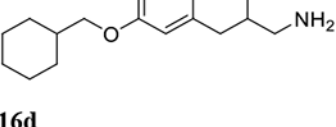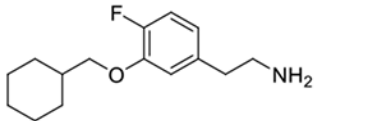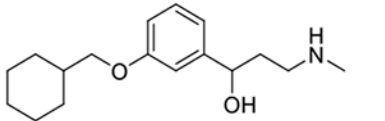
Scheme 4: Synthesis of (3-cyclohexylmethoxy)phenylpropan-amines.[a]

[a]Reagents and Conditions: (a) Cyclohexylmethyl bromide, K_2CO_3, DMF, 90 °C, overnight; (b) 2-(prop-2-yn-1)isoindoline-1,3-dione, $Pd(PPh_3)_2Cl_2$, p-(o-tolyl)$_3$, CuI, NEt_3, THF, 55 °C, 24 h; (c) H_2, Pd/C, MeOH, RT, overnight; (d) hydrazine, EtOH, reflux, 4 h; (e) diethyl (cyanomethyl)phosphonate, LDA, THF, −78 to 25 °C, overnight; (f) LAH, THF, 80 °C, 24 h; (g) diethyl (1-cyanoethyl)phosphonate, n-BuLi, THF, −78 to 25 °C, overnight; (h) H_2, Pd/C, MeOH, RT, 36 hr. (j) i) MsCl, NEt_3, ether, −10 to 0 °C, 3 h, ii) $MeNH_2$, 70 °C, 4 h.
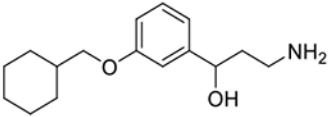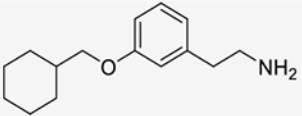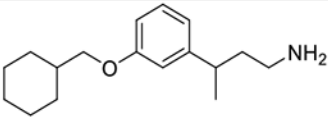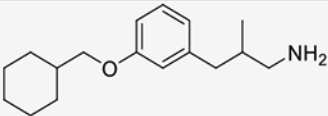
Table 1:

Structures and IC_{50} values of tested emixustat derivatives. Results are expressed as Mean ± SD, n=3.
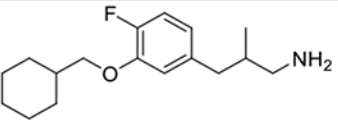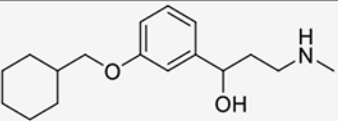
Structure	IC_{50} ± SD (µM)	Structure	IC_{50} ± SD (µM)
3a	0.20 ± 0.02	**6a**	No Inhibition
3b	8.08 ± 3.44	**6b – meta** **6c – para**	No Inhibition
3c	4.67 ± 1.23	**16a**	1.55 ± 0.3
11a	3.19 ± 0.81	**16b**	0.82 ± 0.15
11b	0.42 ± 0.11	**16c**	0.39 ± 0.07
11c	6.73 ± 0.26	**16d**	No inhibition

11d | 1.23 ±
0.13 |
16e | 0.29 ±
0.05 |

Table 2:

Concentrations of 11cRAL and RE in mice eyes quantified by HPLC. Results are expressed as mean ± SD, n = 3 mice.

Group	Time (hours)	Mean ± SD 11cRAL (pmol/eye)	Mean ± SD RE (pmol/eye)
dark adapted	DA	384.1 ± 15.2	67.4 ± 12.4
vehicle	0	22.7 ± 2.6	223.9 ± 20.4
	4	389.5 ± 17.2	58.2 ± 11.0
	24	363.5 ± 26.5	60.0 ± 15.0
3a	0	16.2 ± 16.2	225.1 ± 29.5
	4	22.3 ± 4.0	416.8 ± 86.4
	24	137.4 ± 44.5	377.3 ± 54.5
11b	0	16.0 ± 0.8	254.2 ± 16.7
	4	393.2 ± 18.2	89.5 ± 5.2
	24	406.5 ± 52.9	65.0 ± 24.1
16b	0	25.6 ± 2.7	291.5 ± 33.1
	4	94.4 ± 11.4	435.5 ± 27.5
	24	370.5 ± 9.1	123.9 ± 36.4
16c	0	17.4 ± 0.8	255.5 ± 22.5
	4	323.0 ± 5.1	111.9 ± 18.5
	24	253.5 ± 9.0	85.6 ± 12.7
	0	23.5 ± 2.3	259.9 ± 54.6
	4	413.2 ± 8.1	101.1 ± 12.9

	24	398.0 ± 26.6	122.7 ± 30.6
16d			
	0	13.8 ±1.5	296.6 ± 65.2
	4	22.5 ± 4.5	395.5 ± 60.0
16e	24	201.8 ± 53.2	215.4 ± 99.2

Table 3:

Concentration of tested compounds and their deaminated product in mouse aorta homogenates quantified by HPLC. Results are expressed as mean ± SD, n = 3 technical replicates.

Time	Mean ± SD 3a (μM)	Mean ± SD ACU-5201 (μM)	Mean ± SD 16e (μM)	Mean ± SD ACU-5201 (μM)
0	109.47 ± 4.95	0.00 ± 0.00	100.32 ± 0.95	0 .00 ± 0.00
1	80.53 ± 5.85	19.71 ± 0.29	101.20 ± 0.89	0.48 ± 0.68
4	61.32 ± 2.06	54.81 ± 6.38	89.07 ± 0.49	3.76 ± 0.29

Table 4:

Estimated V_0 of tested compounds in mouse liver microsomes quantified by HPLC. Results are expressed as mean ± SD.

Concentration (µM)	Mean ± SD 3a (pmoles/minute)	Mean ± SD 16e (pmoles/minute)
0	0.00 ± 0.00	0.00 ± 0.00
15	Not tested	23.38 ± 5.32
25	10.08 ± 1.71	54.17 ± 2.78
50	24.05 ± 3.69	64.21 ± 3.84
100	29.67 ± 2.97	89.82 ± 8.70
200	43.92 ± 11.77	97.45 ± 25.77

Table 5:

Pharmacokinetic parameters of tested compounds from testing with liver microsomes. Results are expressed as mean ± SE. C_{int} values are normalized to the grams of protein in the amount of mouse liver microsomes used in assay.

Parameter	Mean ± SE 3a	Mean ± SE 16e
V_{max} (pmol/minutes)	70.85 ± 48.97	119.5 ± 15.99
K_m (pmol/mL)	126.3 ± 192.36	39.01 ± 17.86
C_{int} (L/hour/mg)	0.34± 0.56	1.84 ± 0.88

Table 6:

Quantification of **16e** and **3a** after intraperitoneal injection of **16e** or **3a**.

Quantification of 16e and 3a after single IP of 16e				
Eye			**Serum**	
Time (hours)	**Mean ± SD 16e (pmol / eye)**	**Mean ± SD 3a (pmol / eye)**	**Mean ± SD 16e (pmol / mL serum)**	**Mean ± SD 3a (pmol / mL serum)**
1	39.378 ± 7.7.270	17.075 ± 7.885	750.426 ± 196.201	52.341 ± 9.247
4	7.609 ± 0.235	19.454 ± 6.889	111.115 ± 43.873	79.502 ± 3.448
24	0.000 ± 0.000	1.329 ± 0.268	0.000 ± 0.000	0.000 ± 0.000
Quantification of 16e and 3a after single IP of 3a				
Eye			**Serum**	
Time (hours)	**Mean ± SD 16e (pmol / eye)**	**Mean ± SD 3a (pmol / eye)**	**Mean ± SD 16e (pmol / mL serum)**	**Mean ± SD 3a (pmol / mL serum)**
1	0.000 ± 0.000	131.992 ± 4.437	0.00 ± 0.000	840.957 ± 189.280

Abbreviations: IP (intraperitoneal).

Table 7:

X-ray crystallographic data collection and refinement statistics

	RPE65-compound 16e
Data collection	
Beamline	NECAT ID-E
Wavelength (Å)	0.97910
Space group	$P6_522$
Unit cell dimensions	
a, c (Å)	176.82, 86.20
Resolution (Å)	50-2.10 (2.23-2.10) [*]
R_{merge} (%)	17.6 (233.8)
$I / \sigma I$	10.3 (1.1)
Completeness (%)	99.9 (99.8)
Redundancy	12.7 (13.0)
Wilson B-factor (Å^2)	46.6
Refinement	
Resolution (Å)	48.1-2.1
No. reflections	44,331 (2,261)[†]
R_{work} / R_{free} (%)	17.8/21.1
No. atoms	4,473
Protein	4,071
Iron	1
Water	346
Ligands	20 (compound **16e**), 18 (PLM)
B-factors (Å^2)	46.4
Protein	45.7
Iron	37.7
Water	52.1
Ligand	69.2 (compound **16e**), 64.3 (PLM)
R.M.S. deviations	
Bond lengths (Å)	0.004
Bond angles (°)	1.073
Ramachandran plot	
Favored (%)	97
Number disallowed	0

[*] Highest-resolution shell is shown in parentheses.

[†] Reflections used for cross-validation